

AERODYNAMIC COMPARISONS OF MEMBRANE WINGS
WITH CAMBERED AND FLAT FRAMES
AT LOW REYNOLDS NUMBER

by

ANDREW HARLEY WRIST

JAMES PAUL HUBNER, COMMITTEE CHAIR
CHARLES O'NEILL
DAVID MACPHEE

A THESIS

Submitted in partial fulfillment of the requirements
for the degree of Master of Science in the Department
of Aerospace Engineering and Mechanics
in the Graduate School of
The University of Alabama

TUSCALOOSA, ALABAMA

2016

Copyright Andrew Harley Wrist 2016
ALL RIGHTS RESERVED

ABSTRACT

The limited size of micro air vehicles (MAVs) requires small power sources, leading to a need for high aerodynamic efficiency. Flexible membrane wings at the MAV scale can experience improved lift/drag ratios, delays in stall, and decreased time-averaged flow separation when compared to rigid wings. This research thesis examines the effect of frame camber on the aerodynamic characteristics of membrane wings. The frames for the wings were designed in SolidWorks and constructed using an Objet30 Pro 3D printer. The membranes are composed of silicone rubber. Tests were conducted in The University of Alabama's low-speed wind tunnel in 135 Hardaway Hall in low Reynolds number flow ($Re \sim 50,000$). Aerodynamic force and moment measurements were acquired at angles-of-attack varying from -4 to 24° . The results were used to determine whether cambered frames provide membrane wings with aerodynamic advantages when compared to those with flat frames. Additionally, a digital image correlation (DIC) camera system was used to acquire time-averaged shapes for the membrane wings during wind tunnel tests. The wings were mounted vertically at angles-of-attack of 6° and 18° to represent the regions of maximum efficiency and approaching stall, respectively. An in-house MATLAB program was developed to average the deflection plots from the images and produce time-averaged shapes. Lifting-line theory was applied to the time-averaged shapes to calculate theoretical lift and induced drag coefficients. The experimental set-up, results, and conclusions are discussed.

DEDICATION

To my parents and family

LIST OF ABBREVIATIONS AND SYMBOLS

A	=	Lifting-line theory coefficient
AR	=	Aspect ratio
b	=	Length of span or width of beam
b'	=	Membrane cell span
c	=	Length of chord
c'	=	Membrane cell chord
C_D	=	Drag coefficient
C_{Dv}	=	Induced drag coefficient
C_L	=	Lift coefficient
C_{Lmax}	=	Maximum lift coefficient
$C_{L,\alpha}$	=	Lift-curve slope
C_M	=	Pitching moment coefficient about $c/4$
D	=	Drag force
E	=	Modulus of elasticity
F	=	Force
f	=	Frequency
h	=	Height
I	=	Moment of inertia
L	=	Lift force, beam length
L/D	=	Lift-to-drag ratio, Aerodynamic efficiency
LE	=	Leading edge
M	=	Moment
n	=	Iteration
P	=	Static pressure

P_{amb}	=	Ambient pressure
P_0	=	Total (stagnation) pressure
q_∞	=	Freestream dynamic pressure
R	=	specific gas constant
Re	=	Reynolds number
St	=	Strouhal number
TE	=	Trailing edge
T_{amb}	=	Ambient temperature
t	=	Membrane thickness
U_∞	=	Freestream velocity
u	=	Velocity
x, y, z	=	Cartesian wind tunnel coordinates
α	=	Angle-of-attack
α'	=	Corrected angle-of-attack
ε	=	Membrane strain
ε_0	=	Membrane pre-strain
ε_α	=	Aerodynamically induced strain
δ	=	Deflection angle
Γ	=	Circulation
ϕ	=	Spanwise location
ρ	=	Density
ρ_m	=	Membrane density
Π_1	=	Vanishing membrane tension aeroelastic parameter
Π_2	=	Vanishing material stiffness aeroelastic parameter
σ	=	Bending stress
θ	=	Offset load cell angle

ACKNOWLEDGEMENTS

First, I would like to thank my advisor, Dr. James P. Hubner, for everything he has done for me since I joined his research team in 2012. Since then, under his guidance, I have come across opportunities and success that were likely not possible without his mentorship and dedication. Dr. Hubner is one of the best professors and people I have had the privilege to work with, and I truly appreciate everything he has done to help me get to where I am today – both as a professional and a person. I would also like to thank Dr. Charles O’Neill and Dr. David MacPhee for serving on my committee. I would like to thank David Pepley for his assistance with this project. Particular thanks to my friend and former colleague, Dr. Zheng Zhang, for his help not only with this project, but also throughout most of my work with the membrane wing research. His knowledge and guidance was critical to my growth as a researcher. Thank you to Dr. Jialai Wang for allowing me to use his digital image correlation equipment. Special thanks to Doug Cannon of the 3D printing lab, and Timothy Connell, James Yarbrough, Bobby “Jim” Edmonds, Sam Tingle, and Kenneth Dunn of the machine shop for their fast and reliable assistance with fabricating parts necessary for this study. I would like to acknowledge the funding support from the Department of Aerospace Engineering and Mechanics, The University of Alabama, and the National Science Foundation. Finally, I would like to thank all of my family and friends for their support.

CONTENTS

ABSTRACT.....	ii
DEDICATION.....	iii
LIST OF ABBREVIATIONS AND SYMBOLS.....	iv
ACKNOWLEDGEMENTS.....	vi
CONTENTS.....	vii
LIST OF TABLES.....	ix
LIST OF FIGURES.....	x
CHAPTER 1. INTRODUCTION.....	1
CHAPTER 2. BACKGROUND.....	6
CHAPTER 3. METHODOLOGY.....	20
3.1 FACILITIES.....	20
3.1.1 MAV Wind Tunnel.....	20
3.1.2 Luminescence Imaging Laboratory.....	23
3.1.3 3D Printing Lab.....	24
3.2 TEST ARTICLES.....	28
3.3 DATA ACQUISITION.....	34

3.4 Digital Image Correlation	40
CHAPTER 4. RESULTS AND DISCUSSION.....	43
4.1 Introduction	43
4.2 Experimental Force and Moment Measurements.....	43
4.2.1 Varying Maximum Camber	44
4.2.2 Varying Maximum Camber Location.....	48
4.2.3 Varying Frame Thickness	51
4.3 Time-Averaged Shape Theoretical Analysis	55
CHAPTER 5. CONCLUSIONS	70
REFERENCES.....	73
APPENDIX.....	76
A.1 OFFSET LOAD CELL ANGLE CALCULATION	76
A.2 DIC TIME AVERAGE AND LIFTING LINE THEORY	77
A.3 CIRCULATION TERMS CALCULATION	85

LIST OF TABLES

Table 3.1. Test Specimens 30

Table 4.1. Induced Drag Calculations 69

LIST OF FIGURES

Figure 1.1. Aerovironment Wasp [31]	2
Figure 1.2. 2-Cell, 1-batten membrane wing structure.....	4
Figure 2.1. Endurance of modern MAVs [1]	6
Figure 2.2. Rigid flat vs cambered low-AR wings [20]	8
Figure 2.3. Flow visualization for an AR = 1 wing at Re = 10,000 [30]	9
Figure 2.4. PIV results for rigid plate (top) and membrane wings at A = 12° and B = 16° [11]	10
Figure 2.4. Membrane geometry: unscalped trailing edge (top) and scalped trailing edge at 12.5%, 25%, and 37.5% (bottom, left to right) of cell span [15]	12
Figure 2.5. Trailing edge scallop of a bat [6].....	12
Figure 2.5. Lift coefficient vs. angle-of-attack for membrane wings with varying stiffness [7] ...	13
Figure 2.6. Batten reinforced flexible wing MAV [7]	14
Figure 2.7. Undeformed (left) and deformed (right) surface of a perimeter reinforced membrane wing at $\alpha = 22^\circ$ [8]	15
Figure 2.8. Strouhal number trend vs. Reynolds number [15].....	17
Figure 2.9. Membrane wing models. Left to right: one, two, and three cells. Top to bottom: pre-strain of 4%, 2%, and 1% [14]	18
Figure 3.1. Centerline turbulence intensity in the MAV test section [12]	21
Figure 3.2. MAV Wind Tunnel Test Facility.....	21
Figure 3.3. Wind tunnel test section	23

Figure 3.4. Objet30 Pro 3D printer	24
Figure 3.5. VeroBlue material properties [28].....	26
Figure 3.6. Bending beam test setup.....	26
Figure 3.7. Bending beam test results.....	27
Figure 3.8. Stratasys Dimension SST 1200es 3D printer.....	28
Figure 3.9. Top view of frames without membrane. Dimensions are in inches	29
Figure 3.10. Top: 3D-printed NACA 4504 frame for a membrane MAV wing. Bottom: Cross-section for 3D-printed frame	30
Figure 3.11. Top: Top view and Bottom: side view of attaching the membrane to a NACA 4504 frame.....	32
Figure 3.12. NACA-designated airfoils tested.....	33
Figure 3.13. Test articles.....	33
Figure 3.14. Test article/traverse setup [12]	35
Figure 3.15. Load cell DAQ system for aerodynamic force measurement [12]	36
Figure 3.16. Offset load cell angle when the model is set to zero angle of attack	37
Figure 3.17. Load cell offset angle calculation	37
Figure 3.18. Process for aerodynamic coefficient plot generation using the LabVIEW Program, Acquire Lift and Drag.vi.....	39
Figure 3.19. Front panel of Acquire Lift and Drag.vi	39
Figure 3.20. DIC system setup	40
Figure 3.21. Spray-painted speckle pattern	41
Figure 3.22. Correlated Solutions displacement analysis software. (a) is the geometry selection procedure, while (b) is the displacement plot output.....	42
Figure 4.1. Plots for C_L and C_D with varying frame camber	46

Figure 4.2. Plots for L/D and $C_L^{3/2}/C_D$ with varying frame camber	47
Figure 4.3. Plot for $C_M c/4$ with varying frame camber	48
Figure 4.4. Plots for C_L and C_D with varying maximum camber location on frame.....	49
Figure 4.5. Plots for L/D and $C_L^{3/2}/C_D$ with varying maximum camber location on frame.....	50
Figure 4.6. Plot for $C_M c/4$ with varying maximum camber location on frame.....	51
Figure 4.7. Plots for C_L and C_D with varying frame thickness	52
Figure 4.8. Plots for L/D and $C_L^{3/2}/C_D$ with varying frame thickness	53
Figure 4.9. Plot for $C_M c/4$ with varying frame thickness	54
Figure 4.10. Symmetric spanwise lift distribution.....	56
Figure 4.11. MATLAB code structure.....	58
Figure 4.12. Effect of third-degree polynomial fit on the trailing edge on the NACA 4504 frame	59
Figure 4.13. Local chord and effective angle-of-attack.....	60
Figure 4.14. Lifting-line analysis flow chart	60
Figure 4.15. Lift coefficient at 6°	61
Figure 4.16. Time-averaged shapes at 6° (side view on left, top view on right). From top to bottom: 2504, 4504, 6504. Flow is from right to left. Red indicates more deflection, while blue indicates little to no deflection.....	62
Figure 4.17. Lift coefficient at 18°	63
Figure 4.18. Time-averaged shapes at 18° (side view on left, top view on right). From top to bottom: 2504, 4504, 6504. Flow is from right to left.....	64
Figure 4.19. Time-averaged and spanwise-averaged shape side views for membrane wings from top to bottom: flat, 2504, 4504, and 6504 airfoils. Flow is from right to left	67
Figure 4.20. $C_{L,max}$ vs additional membrane camber	68

CHAPTER 1. INTRODUCTION

The 20th century was dominated by manned aircraft and spacecraft. As the century progressed, airplanes grew larger, became safer, and carried more people. Towards the end of the century, focus began to shift from large, manned to smaller, unmanned aircraft because of their functionality in civilian, military, and homeland security objectives. Over the past 40 years, unmanned air vehicles (UAVs) have quickly become prevalent in the aerospace industry. UAVs are commonly used in military situations for reconnaissance and targeting missions. They are also available commercially for agriculture, rescue, hobby, and other uses [1-2].

In the 1990s, the Defense Advanced Research Projects Agency (DARPA) presented a new challenge. Due to limitations in certain operational environments for larger UAVs, the development of a small-scale UAV was desired. This new class of UAV, known as a micro air vehicle (MAV), has no length dimension greater than 6 in with a gross takeoff weight of approximately 200 g [1]. Limiting factors to the development of MAVs include flight efficiency, available power, and size. MAVs operate in a low Reynolds number of 100,000 or less. Airfoils traditionally used in higher Reynolds number flows experience decreases in aerodynamic efficiency in this Reynolds number regime. Aerodynamic characteristics are not as well-known at this range, leading to a necessity for more research. MAVs also require smaller power sources to decrease weight and maximize efficiency. Due to the reduced power availability, a need for aerodynamic efficiency is even greater.

There are three main types of MAVs. Each offer their own advantages and disadvantages. Rotor-wing MAVs, such as quadcopters and helicopters, have the ability to hover but experience decreases in efficiency due to low Reynolds number effects and available power-to-weight ratios, despite lower disk loading [1]. They generate lift by creating a downward thrust with rotors. Flapping-wing MAVs, or ornithopters, generate lift and thrust from the mechanical flapping motion of the wings. This enables increased maneuverability but also decreases efficiency due to the heavier and energy draining flapping mechanisms [3]. The third classification of MAVs, fixed-wing MAVs, separate the thrust and lift devices similar to traditional aircraft and are often designed with rigid wings and airframes. The fixed-wing configuration provides MAVs with the best energy efficiency in forward flight, non-hover conditions [1, 4]. An example of a fixed-wing MAV is shown in Figure 1.1.



Figure 1.1. Aerovironment Wasp [1]

With the rapid decreases in aerodynamic efficiency experienced by flow characteristics where $Re < 100,000$, researchers have looked to nature for answers, where natural flyers have evolved for millions of years to optimize flying in this Reynolds number regime. Certain birds have features that provide them with aerodynamic benefits in low Reynolds number flow [5]. Additionally, bat wings are composed of a flexible material that is not typically seen on wings in the Reynolds number range above 100,000. The additional flexibility observed with bat wings provides aerodynamic advantages, allowing them to fly for longer periods of time using less energy [6].

Bat wings resemble a thin membrane-like material with a fixed leading edge and free, scalloped trailing edge. Researchers at Brown University confirmed that this flexible wing configuration provides the bat with increased aerodynamic efficiency [6]. Previous studies concluded that applying a similarly flexible membrane material to a fixed-wing-type MAV wing increases aerodynamic efficiency when compared with rigid wings [7-12]. Studies, including some at The University of Alabama, have further investigated the use of membrane wings and have optimized cell geometries, membrane pre-strain, and trailing edge scallop characteristics for better aerodynamic efficiency [7, 13-17]. Typically, these membrane wings are composed of a rigid frame and a silicon rubber (or similar) membrane, as shown in Figure 1.2. Spanwise “battens” divide the wing into cells and are often implemented to increase overall wing stiffness.

Membrane wing studies have focused primarily on flat-frame geometries with little emphasis on the effect of added frame camber. In this thesis, a study of membrane wings with

frames of varying camber is presented to determine their effectiveness in comparison to membrane wings with flat frames.

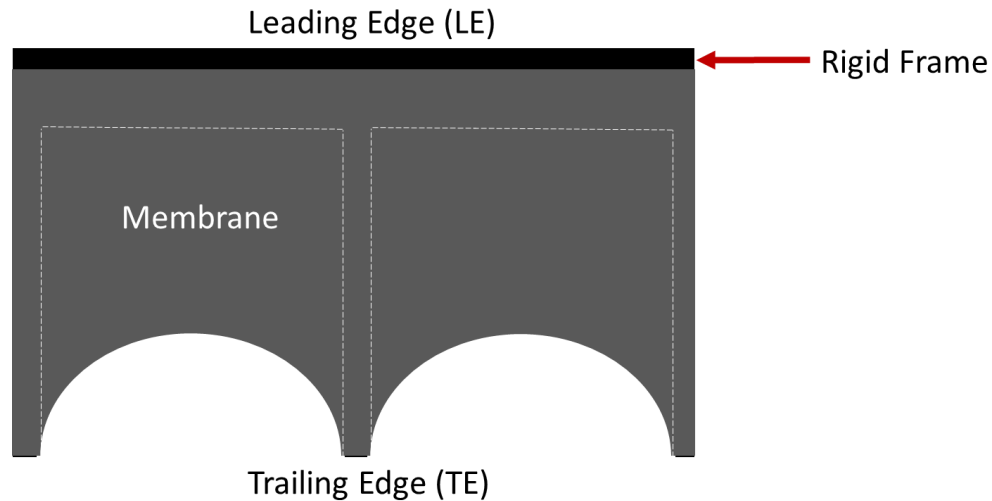


Figure 1.2. 2-Cell, 1-batten membrane wing structure

The objectives of this thesis are:

- to measure the aerodynamic forces for flexible membrane wings with cambered frames and determine whether they are more efficient than membrane wings with flat frames,
- to obtain time-averaged shapes of the membrane wings during test conditions and compare trends between frame camber and membrane shape, and
- to correlate changes in aerodynamic forces with time-average membrane shapes using lifting-line theory calculations.

The literature review in Chapter 2 offers a detailed examination of previous rigid and flexible MAV wing studies. Numerous aerodynamic force measurements have been conducted to gain better understanding of the effect on MAV wing aerodynamics when $Re < 100,000$.

Chapter 2 will conclude with a summary of previous membrane wing tests conducted at The University of Alabama that would ultimately lead to the work presented in this thesis. Tests were conducted in The University of Alabama's low-speed Wind Tunnel in 135 Hardaway Hall, where equipment and necessary instrumentation is available for performing aerodynamic force measurements on MAV wings at angles-of-attack varying from -4 to 24° . Additionally, a DIC camera system was borrowed from Dr. Jialai Wang of the Civil Engineering department to obtain images to produce time-averaged shapes for the test subjects. The experimental facilities and setup are further detailed in Chapter 3. Chapter 4 presents the experimental results for the aerodynamic force measurements. Additionally, Chapter 4 discusses the code developed for theoretical analysis of the time-averaged shapes and its results. Lastly, Chapter 5 presents the general conclusions of the study. The results from this study can be ultimately applied to the improvement of aerodynamic efficiency for fixed-wing MAVs.

CHAPTER 2. BACKGROUND

When Pines and Bohorquez [1] outlined the challenges facing future MAV development, developing a better understanding for low Reynolds number aerodynamics was described as one of the key advancements needed for improving MAV flight efficiency. Modern MAVs still fall short of the endurance target of 60 minutes [1], as shown in Figure 2.1.

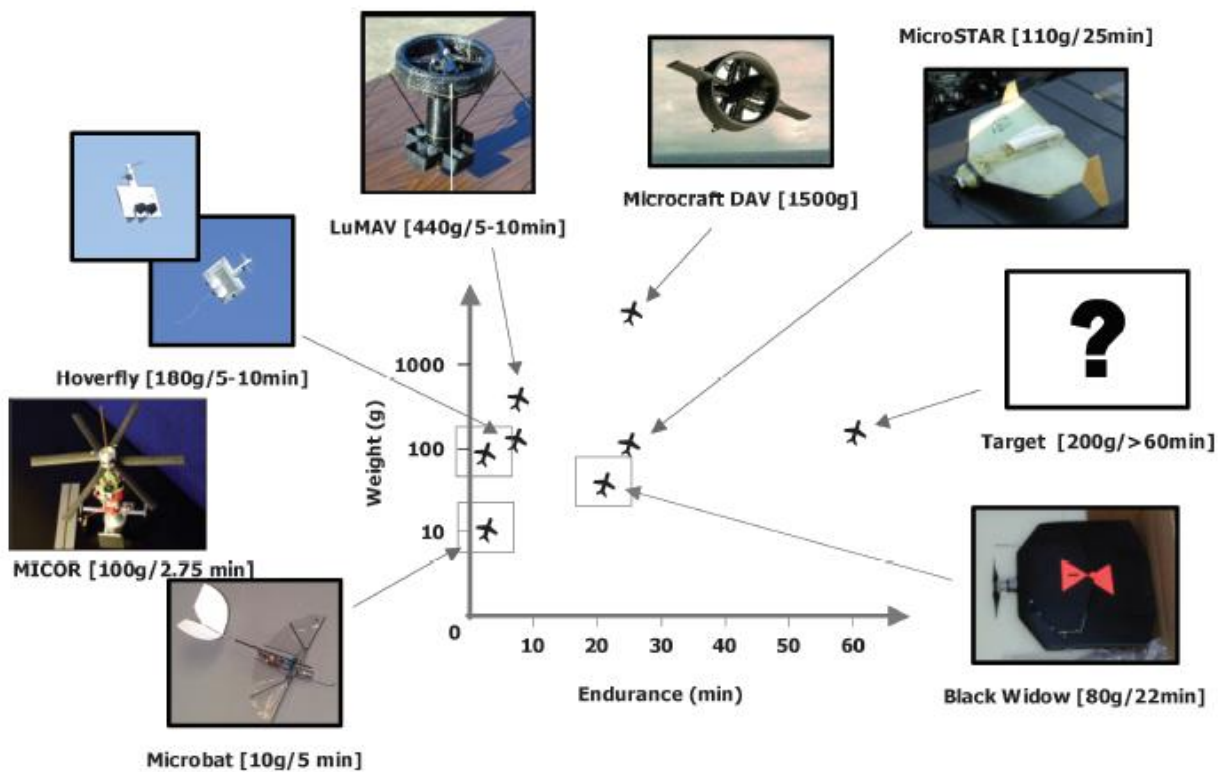


Figure 2.1. Endurance of modern MAVs [1]

Endurance of a fixed-wing MAV is proportional to $C_L^{3/2}/C_D$. Therefore, understanding how various wing characteristics affect lift and drag for MAVs is critical for improving their endurance. Thus, experimental aerodynamicists have focused on improving aerodynamic measurements in low Reynolds number conditions.

The lack of suitably accurate testing techniques has historically presented challenges to researchers obtaining experimental force measurements for low aspect ratio wings in low Reynolds number test conditions [18]. Over the last few decades, improvements in wind tunnel testing equipment, including relatively inexpensive load cells, have allowed for higher accuracy aerodynamic force measurements when $Re < 200,000$ than previously available [19-21]. This increased accuracy for measurements in lower Reynolds number flows has resulted in the progression of MAV wing research. Mueller [19] detailed the necessity for the use of sensitive equipment when acquiring aerodynamic measurements on small models at low Reynolds numbers. Tests were performed on cambered and flat plate wings for given Reynolds numbers, and variations were detected in maximum lift coefficient. Variations such as these were not detectable in Zimmerman's work [18] before more up-to-date testing techniques existed.

Torres and Mueller [21] studied the influence of wing planform, aspect ratio, and Reynolds number on low aspect ratio wings. In the study, rectangular, Zimmerman, inverse Zimmerman, and elliptical planforms were developed and tested with aspect ratios of 0.50 to 2.00, increasing by 0.25. Results indicated that different planforms were more effective at different aspect ratios. For higher AR values, elliptical planforms experienced higher maximum lift coefficients, while inverse Zimmerman wings were more favorable at aspect ratios below 1.0. In comparison, Mizoguchi and Itoh [22] determined that for wings with aspect ratio of 3.0

and above, the effect of aspect ratio on aerodynamic efficiency is not significant. He also noted that wing tip vortices greatly affect the characteristics of wings as aspect ratio approaches 1.0.

To better understand the aerodynamics of low aspect ratio wings in low Reynolds number flow, Pelletier and Mueller [20] offered a comparison of flat and cambered wings at Reynolds numbers between 60,000 and 200,000. As shown in Figure 2.2, the C_{Lmax} for wings with camber, as indicated by the red line, was greater than those of the flat plate wings. As noted earlier, aerodynamic efficiency also decreased with Reynolds number in the study.

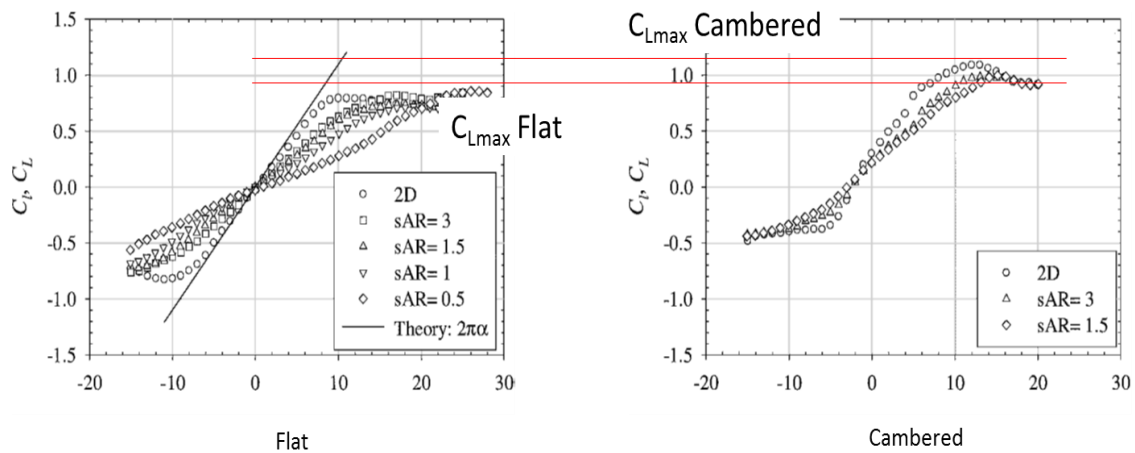


Figure 2.2. Rigid flat vs rigid cambered low-AR wings [20]

Okamoto and Azuma [30] used flow visualization to offer an explanation for the reduction in aerodynamic efficiency in low Reynolds number flow for rigid wings. He showed that for a low aspect ratio wing in low Reynolds number flow, a separation bubble begins at the leading edge and does not reattach, especially at higher angles-of-attack. Additionally, multiple smaller vortices were present outside of the separated region.

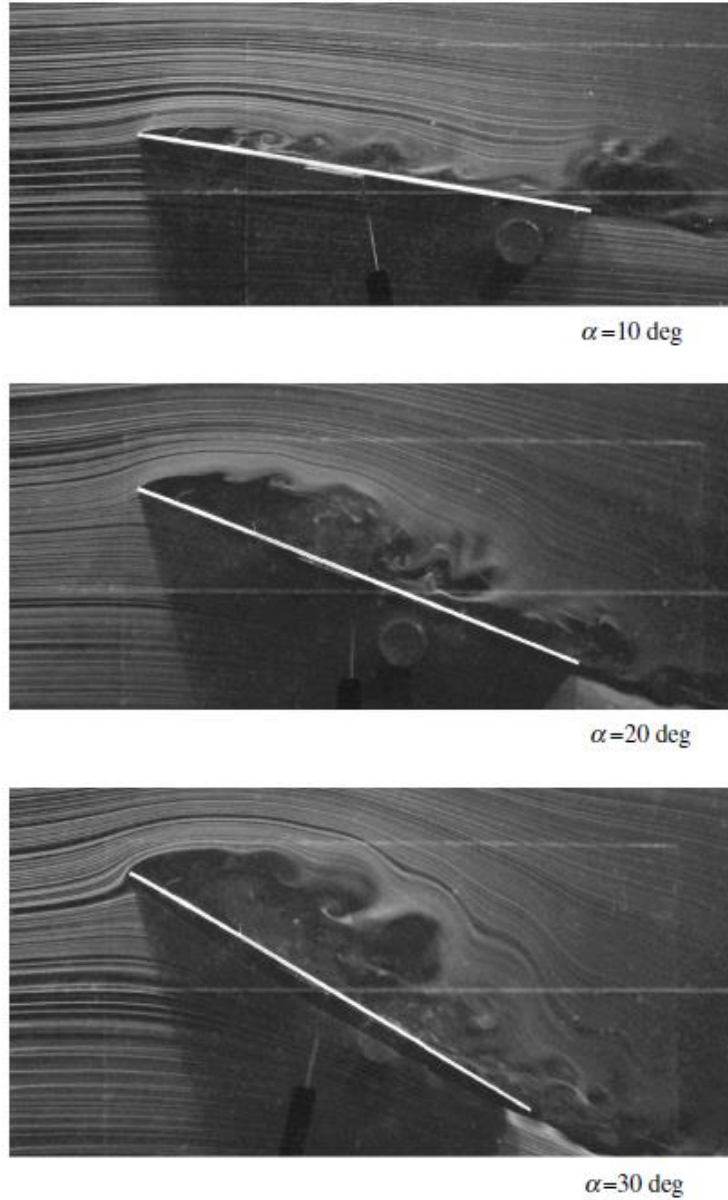


Figure 2.3. Flow visualization for an AR = 1 wing at Re = 10000 [30]

By comparison, Timpe *et al.* [11] used particle image velocimetry (PIV) to capture the time-averaged separation bubble on membrane wings with flow induced vibrations to compare with rigid wings. He found that the flow separation for the membrane wings is less significant and remains more attached than that of the flat plate. The PIV images for this study are

displayed in Figure 2.4, where red indicates higher downstream flow velocity and blue indicates lower velocity reverse flow. The larger blue regions indicate more flow reversal and larger flow separation.

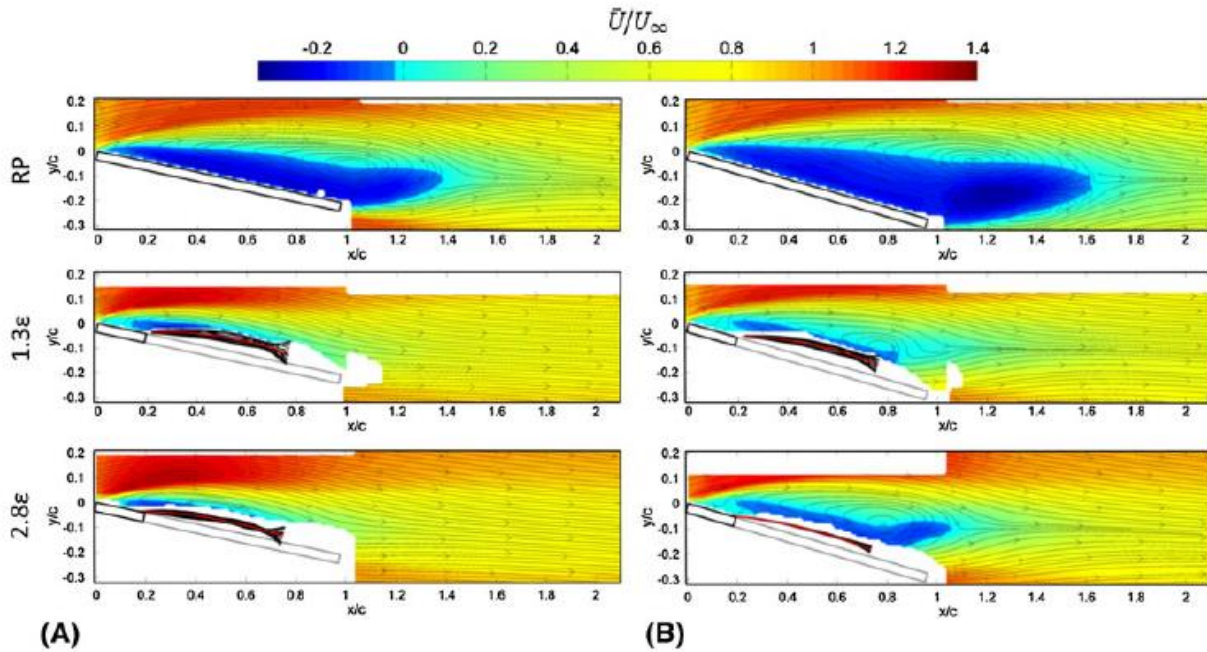


Figure 2.4. PIV results for rigid plate (top) and membrane wings at $A = 12^\circ$ and $B = 16^\circ$ [11]

In addition to decreased flow separation, when compared to low aspect ratio rigid wings in the Reynolds number regime for MAVs, membrane wings can experience improved lift/drag ratios, delays in stall, and stability and control advantages [6-7, 9, 23-24]. The aerodynamic advantages observed with membrane wings are attributed to passive, time-averaged and dynamic deformations that occur as the wing vibrates in flow. To optimize membrane wings for aerodynamic efficiency, a number of various wing geometries and characteristics have been studied.

Timpe *et al.* [11] showed that membrane wings with higher pre-strained membranes experience aerodynamic characteristics closer to flat plates. Zhang *et al.*'s [14] force measurements for membrane wings with varying pre-strain also indicated improvement for membrane wings with less pre-strain. Arce and Ukeiley [13] further investigated the flow fields for membrane and flat plate models and found similar trends. He noted that a membrane wing with 1 percent pre-strain had a smaller separation bubble and wake deficit compared with the 4 percent pre-strain.

In addition to pre-strain, trailing edge characteristics also affect aerodynamic performance. Mastramico and Hubner [10] found that a scalloped, free trailing edge decreases local profile drag when compared to fixed or non-scalloped trailing edges. Hu *et al.* [9] found that the free trailing edge deflects from its original position, causing a reduction in the effective angle-of-attack and delays in stall. However, his non-scalloped trailing edge models also experienced increases in flutter and drag. Hubner and Hicks [15] performed an investigation to determine the benefits of trailing edge scalloping on membrane wings with free trailing edges. He found that the highest lift/drag ratios were obtained with a cell-span scallop of 25%. For this scallop percentage, increasing Reynolds number also increased lift and decreased drag when angles-of-attack exceeded 8° . A diagram for his scalloped and unscalloped test articles is presented in Figure 2.5. The idea of scalloping, as previously mentioned, came from bats as shown in Figure 2.6.

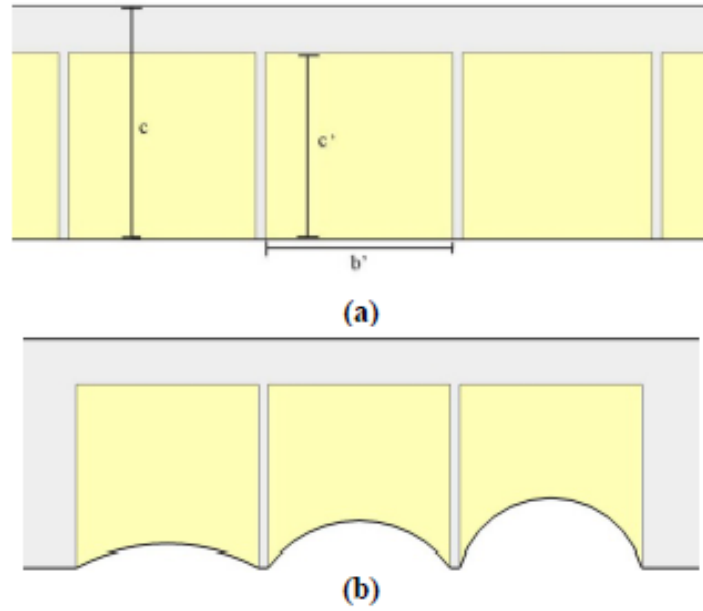


Figure 2.4. Membrane geometry: unscalped trailing edge (top) and scalped trailing edge at 12.5%, 25%, and 37.5% (bottom, left to right) of cell span [15]



Figure 2.5. Trailing edge scallop of a bat [6]m

Ifju *et al.* [7] detailed the use of battens to increase the stiffness of the membrane wings. While the 1-batten membrane wings (larger membrane cell size) experienced further delays in stall when compared with the 2- and 6- batten wings, the 6-batten wing experienced higher lift at lower angles-of-attack. This trend is shown in Figure 2.5. A batten-reinforced wing was successfully tested on a flying platform as shown in Figure 2.6. The frame for the wing is thin and cambered to mimic those of birds and bats.

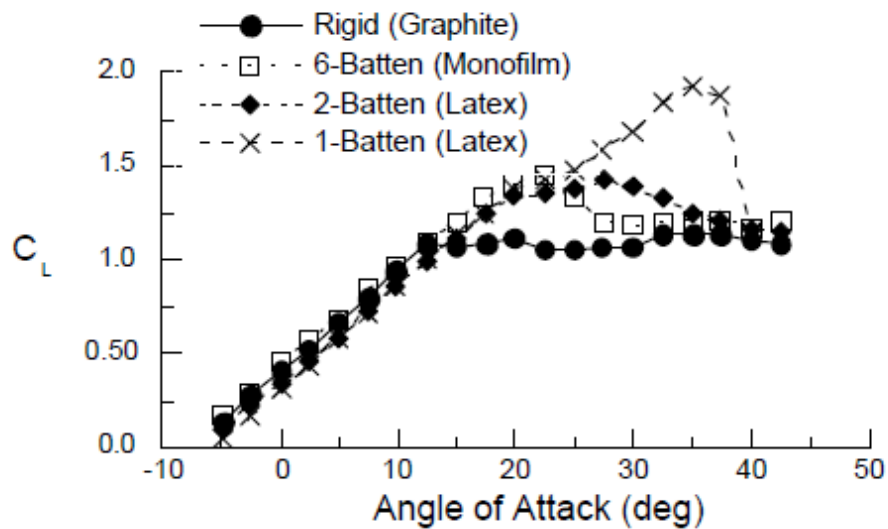


Figure 2.5. Lift coefficient vs. angle-of-attack for membrane wings with varying stiffness and $Re = 60,000$ [7]

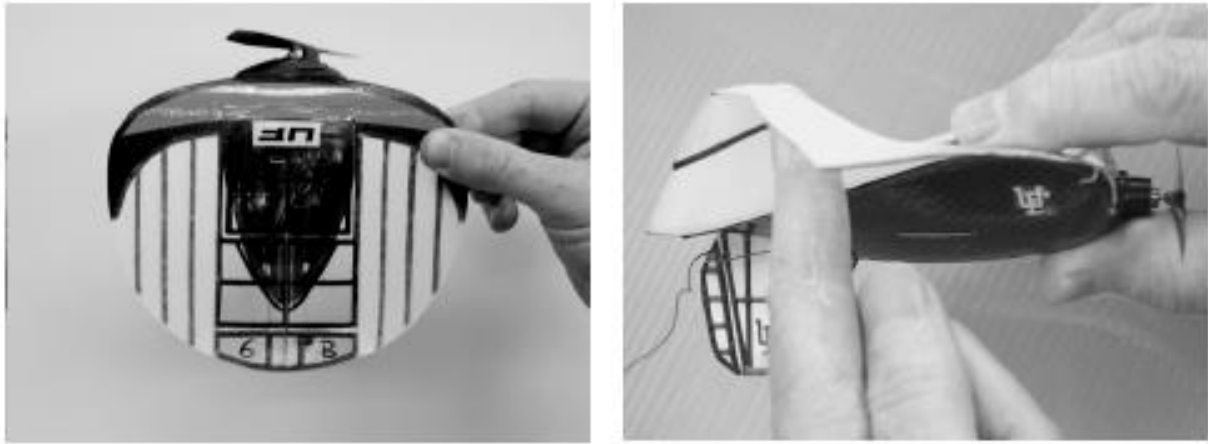


Figure 2.6. Batten reinforced flexible wing MAV [7]

Abuduram *et al.* [17] detailed a series of experimental tests on the effect of batten thickness and spacing. He found that wings with thin battens delay stall and decrease lift slopes. Additionally, wings with thicker battens delayed stall, but also showed larger lift values at higher angles-of-attack. Higher post-stall lift spikes were apparent when increasing the distance between battens. However, larger distances between battens also resulted in a decrease in pre-stall lift. Similar to other studies, trends showed that scalloping the trailing edge removed some of the trailing edge vibration and increased pre-stall lift.

Albertani *et al.* [8] proposed the use of digital image correlation (DIC) to obtain global deformations of a model during wind tunnel tests. He tested a rigid MAV wing along with batten reinforced (free trailing edge) and perimeter reinforced (fixed trailing edge) membrane wings. He found a substantial geometric twist associated with the batten reinforced wing. This geometric twist was found to improve stall and gust alleviation. Alternatively, the perimeter reinforcement affected the aerodynamic twisting (or cambering) the wing, causing increases in lift and longitudinal stability when dynamic pressure and angle-of-attack were changed

dramatically. The undeformed and deformed surface of a perimeter reinforced membrane wing is displayed in Figure 2.7.

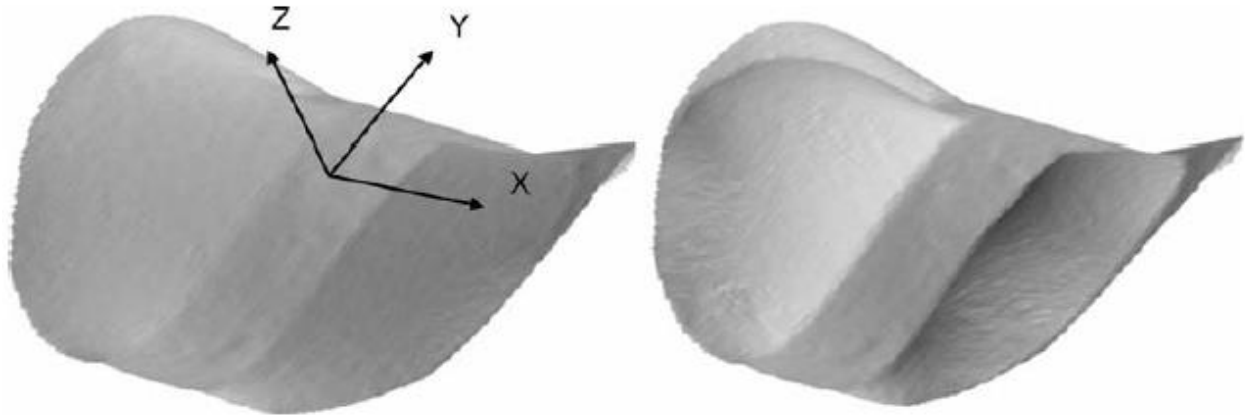


Figure 2.7. Undeformed (left) and deformed (right) surface of a perimeter reinforced membrane wing at $\alpha = 22^\circ$ [8]

Johnston *et al.* [25] studied the effect of the rigid frame on the onset of membrane flutter. From testing various frame configurations with varying membrane pre-strains, experiments concluded that membrane vibration is not an effect of the rigid frame structure. Instead, the membrane vibration and onset of membrane flutter is driven by pre-strain and flow velocity. Scott *et al.* [16] performed direct measurement of membrane vibration velocity with laser vibrometry combined in temporal synchronization with hot-wire anemometry. From testing various cell geometry and materials (latex and silicon rubber), he found that the frequency of small-amplitude vibrations is governed by the material, geometric, and pre-strain characteristics of the membrane. While the energy in the leeside free shear layer help drive the membrane vibration, the frequency of the vibration was set by material properties.

Additionally, he and Wazsak *et al.* [17, 23] both have noted the limited durability with latex material in comparison to monofilm or silicon rubber.

Theoretical modeling has been of interest in more recent studies. Gordnier and Attar [26] found reasonable agreement between experimental methods and a high-order computational method, aeroelastic solver. The solver uses Navier-Stokes equations and an implicit LES scheme to accurately capture the laminar, transitional, and turbulent flowfields for low Reynolds number flows. The fluid solver was paired with a Reissner-Mindlin finite-element plate model to be applied to a flexible membrane wing. Deflection measurements observed from PIV tests were similar to those observed with the computational model.

Hubner and Hicks [15] proposed the use of Strouhal number with a vibrating string analogy to collapse nondimensional frequency relative to Reynolds number. This proposed variation of Strouhal number is given by

$$St_c = \frac{\sqrt{\frac{\rho f}{\rho_m}} c}{\sqrt{tb'}}, \quad (2.1)$$

where f is the peak frequency, c is chord length, ρ_m is membrane density, b' is membrane span, and t is membrane thickness. Figure 2.8 shows that this Strouhal number-based approximation models the results reasonably well.

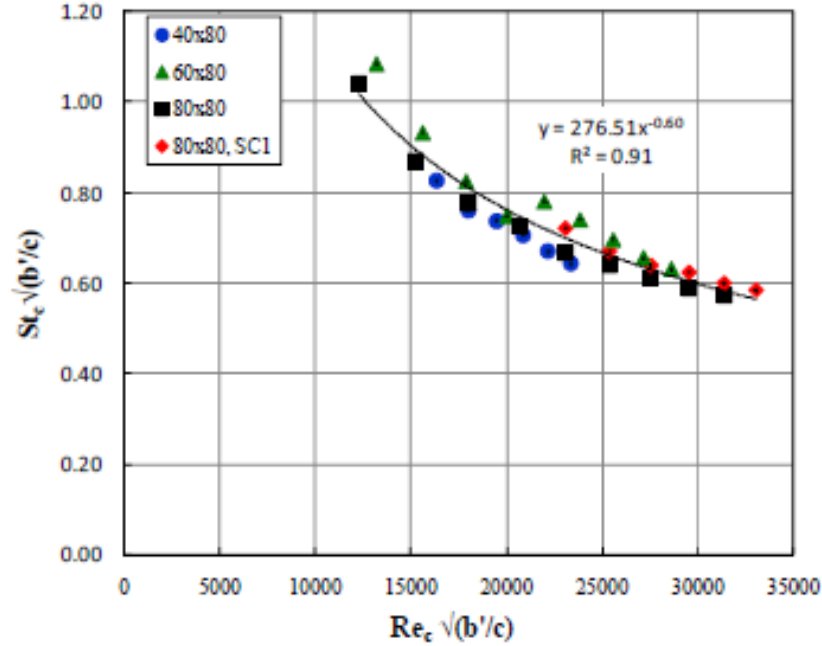


Figure 2.8. Strouhal number trend vs. Reynolds number [15]

Further investigation into trends related to frequency scaling involved an analysis by Zhang *et al.* [27] where a nondimensional vibration frequency scaling relative to a vanishing material stiffness aeroelastic parameter was developed for flat-plate membrane wings at low and moderate angles-of-attack. The proposed aeroelastic loading equation is

$$\Pi_2 = \frac{(\varepsilon_o + \varepsilon_a)Et}{q_\infty b'}, \quad (2.2)$$

where ε_o is pre-tension, ε_a is estimated aerodynamically-induced strain, E is elastic modulus, t is membrane thickness, q_∞ is free-stream dynamic pressure, and b' is membrane cell chord length. Due to strong vortex shading at higher angle of attacks, this proposed scaling is appropriate for moderate to low angles-of-attack.

Zhang *et al.* [14] studied both wing and cell aspect ratio effects of membrane wings and compared results to 3D printed time-averaged shapes of the membrane wings at different angles-of-attack and pre-tensions. The flexible membrane wings, shown in Figure 2.9 (AR = 2), outperformed the rigid, time-averaged shape wings, indicating camber alone was not the sole reason for the benefit. The membrane vibration is also essential for generating the additional lift observed among membrane wings.

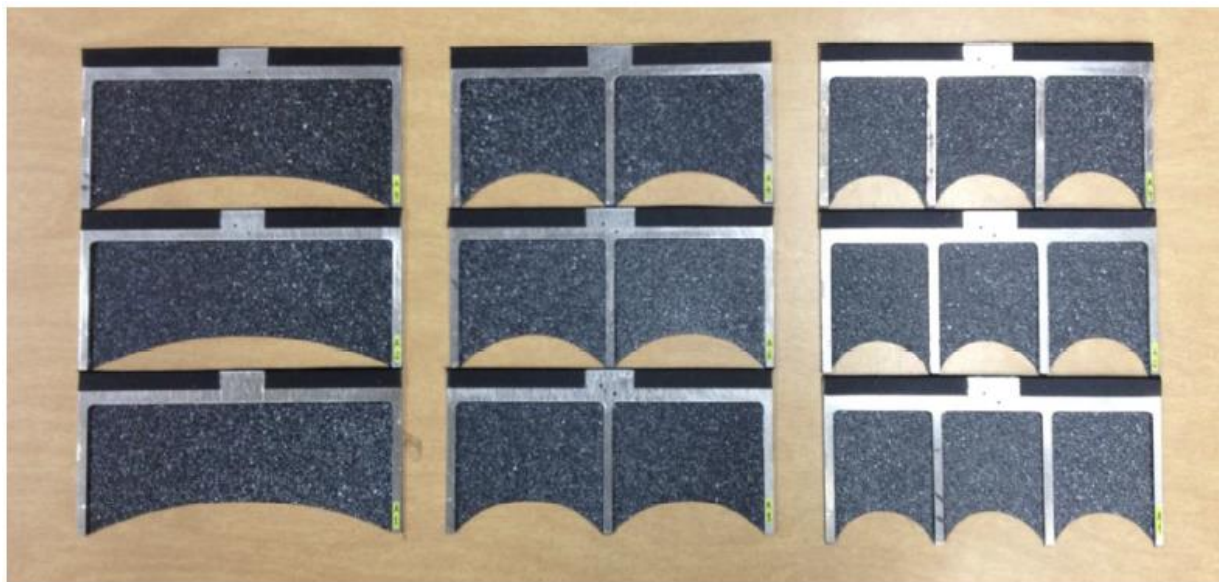


Figure 2.9. Membrane wing models. Left to right: one, two, and three cells. Top to bottom: pre-strain of 4%, 2%, and 1% [14]

As discussed in the section, camber and flexibility are both important characteristics for improving MAV wing performance. However, no study has systematically quantified the effect of frame camber on the aerodynamic performance of low aspect ratio membrane wings. Thus, it is of interest to determine whether applying camber to the frame of a flexible membrane wing would allow for improved aerodynamic performance. This thesis investigates the effects

of applying camber to the frames of membrane wings. Experimentally-obtained, aerodynamic force coefficients are used as a comparison between membrane wings with cambered frames and those with flat frames. Additionally, the membrane wings with cambered frames are compared among each other. Similar to Zhang *et al.* [14], time-averaged shapes are also generated. However, instead of 3D printing the time-averaged shapes for an experimental comparison, lifting-line theory is used to compare experimental and theoretical results.

CHAPTER 3. METHODOLOGY

3.1 FACILITIES

3.1.1 MAV Wind Tunnel

Experiments in this investigation were performed in The University of Alabama's low-speed Wind Tunnel in 135 Hardaway Hall. The tunnel has an open-circuit, interchangeable test section. For this investigation, the 30 in x 30 in (76 cm x 76 cm) test section was used. A second contraction and test section can be installed with a 12 in x 36 in cross-section. The two sections are sometimes referred as the MAV and boundary layer (BL) test sections. The MAV test section is 6 ft (1.83 m) long with 360 degrees of optical access. The flow velocity ranges from 4.5 to 49.2 mph (2.0 to 22.0 m/s) with an uncertainty of ± 0.67 mph (0.3 m/s) [12]. The centerline free stream turbulence intensity is less than 0.5% at 10 m/s, as shown in Figure 3.1, but slightly higher at higher speeds. The tunnel can be equipped with instruments suitable for hotwire anemometry, digital pressure scanning and sensing, data acquisition devices, force measurement systems, traversing systems, high speed imaging, and more. A schematic of the wind tunnel facility is presented in Figure 3.2.

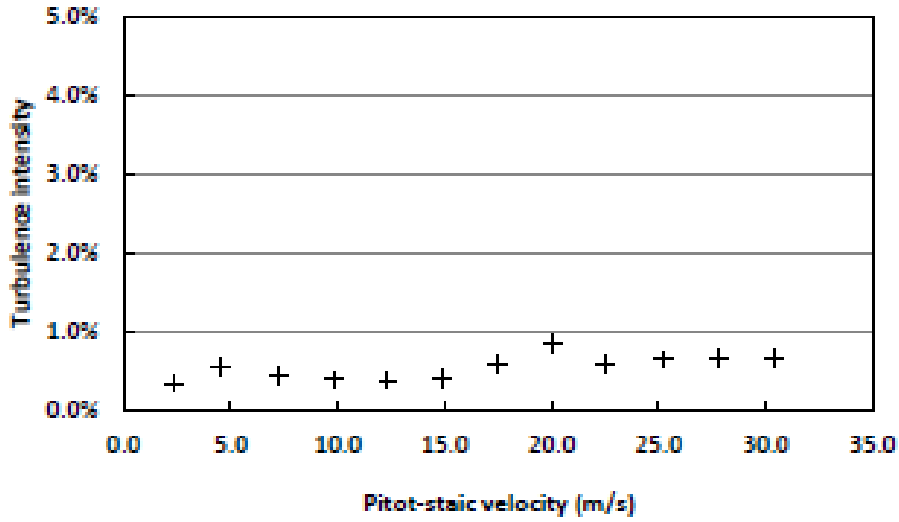


Figure 3.1. Centerline turbulence intensity in the MAV test section [12]

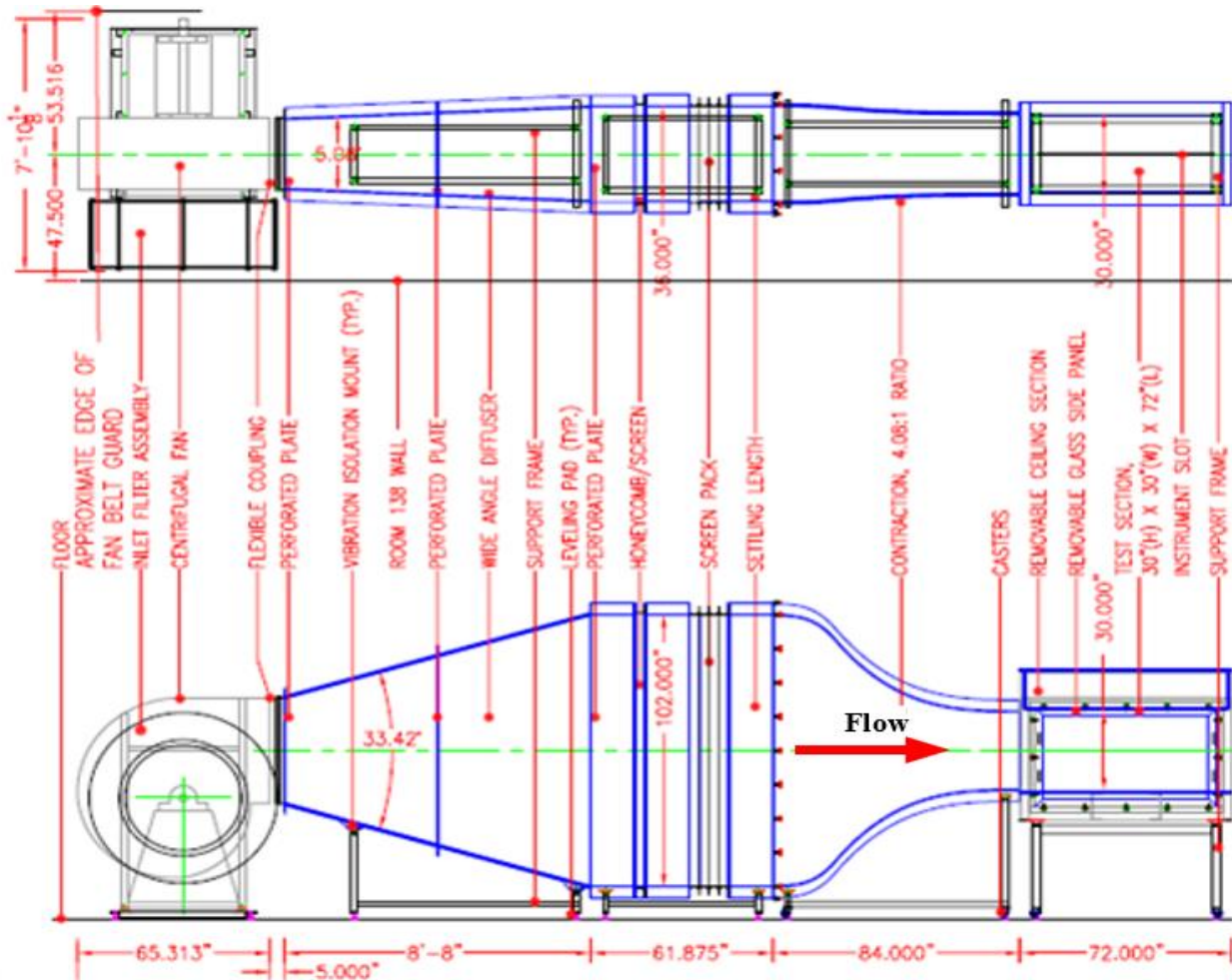


Figure 3.2. MAV Wind Tunnel Test Facility

The freestream velocity was recorded throughout wind tunnel tests using a Pitot-static probe. Static and stagnation pressures were measured by a Pitot-static tube and a digital pressure scanner (NetScanner PSI-9116, ± 5 kPa range). Air density was calculated using the ideal gas law for dry air conditions (Eq. 3.1). For this calculation, ambient absolute pressure and temperature were measured by a Druck DPI-142 digital barometer and K-type thermocouple connected to a National Instruments USB-9211 module, respectively.

$$\rho = \frac{P_{amb}}{RT_{amb}} \quad (3.1)$$

In Equation 3.1, P_{amb} is the ambient pressure, T_{amb} is the ambient temperature, and R is the specific gas constant, 287 J/(Kg·K). The density, ρ , is substituted into Bernoulli's equation to determine freestream velocity,

$$U_{\infty} = \sqrt{2(P_o - P)/\rho} \quad (3.2)$$

where P_o is stagnation pressure and P is static pressure as measured by the Pitot-static probe. The estimated bias-based error for the freestream velocity is ± 0.3 m/s [12]. A diagram of the wind tunnel test section with a model installed is shown in Figure 3.3.

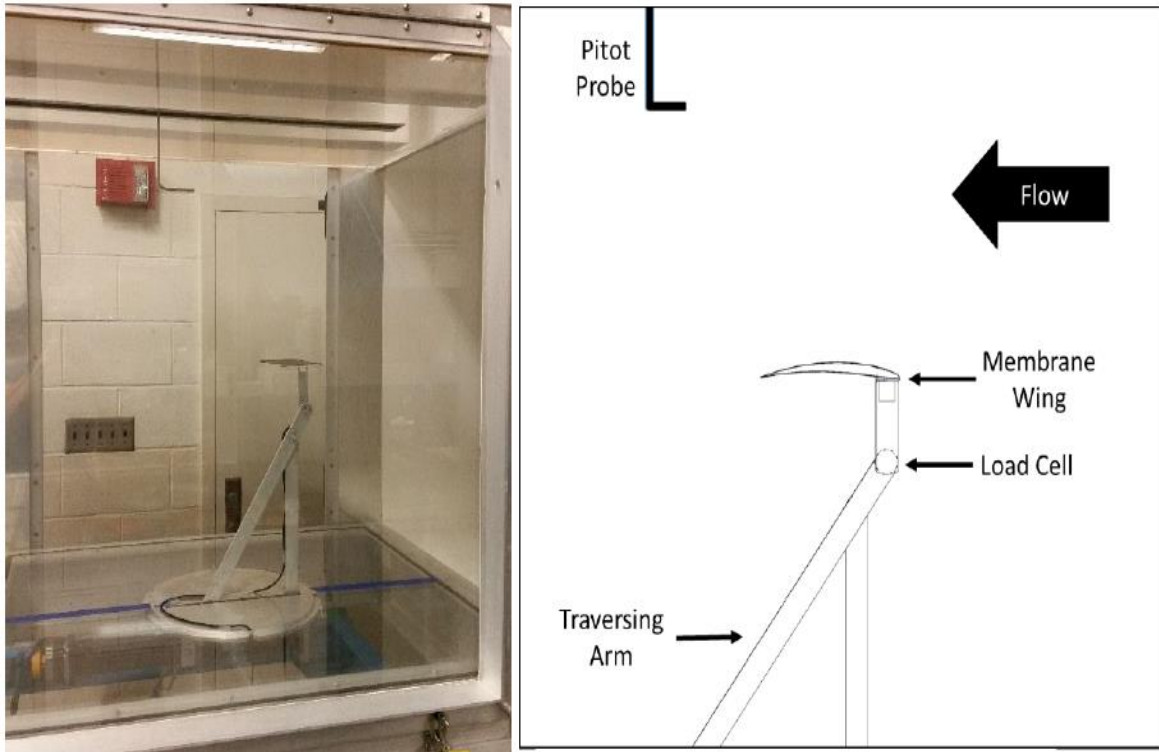


Figure 3.3. Wind tunnel test section

3.1.2 Luminescence Imaging Laboratory

Room 140 Hardaway Hall, known as the Luminescence Imaging Laboratory, houses the materials and instruments necessary for specimen preparation and experimental test setup. The facility includes high speed imaging equipment, UV lamps, PC-based work stations, data acquisition equipment, a coordinate measurement machine, linear actuators, work benches, and other tools and testing equipment. Tests performed in this lab include the bending beam and membrane properties tests discussed in Section 3.1.3.

3.1.3 3D Printing Lab

The College of Engineering's UA 3D Printing Lab, part of the College of Engineering's student workspace called The Cube, houses six 3D printing machines that are capable of printing objects with a range of dimensions, materials, and accuracies suitable for various applications. The two printers primarily used for this research were the Objet30 Pro and Stratasys Dimension SST 1200es.



Figure 3.4. Objet30 Pro 3D printer

The Objet30 Pro is a commercial-grade 3D printer capable of accuracies down to 6×10^{-4} in (0.01 mm) on a build table of 11.57 x 7.55 x 5.85 in (294 x 192 x 149 mm). The printer uses a photopolymer material called vero. The properties for this material are detailed in Figure 3.5. The quoted modulus of elasticity for the material is 290-430 ksi (2000-3000 MPa). However,

from an in-house designed bending beam test, the modulus of elasticity was measured at approximately 130 ksi (900 MPa). To measure the modulus of elasticity, a 0.5 x 0.5 x 3.5 in (1.3x1.3x8.9 cm) beam was printed using the VeroBlue material and tip deflections were measured when known weights were applied at the tip. The specimens were clamped at one end. A weight platform was suspended from the opposite end of the beam. A Pixis 1024 camera was used for acquiring images of the tip of the beam at loads of 50 g, 100 g, and 150 g. Subsequently, a LabVIEW program was written to determine the deflection of the beam at each weight. The program measures the number of pixels displaced by the beam in a given set of images. The experimental setup for the bending cantilever beam test is shown in Figure 3.6, while the test results are shown in Figure 3.7. Six specimens were tested—three of which were cured with a UV lamp. Bending stress and applied strain were calculated from Equations 3.3 and 3.4, respectively.

$$\sigma = \frac{My}{I} \quad (3.3)$$

$$\varepsilon = \frac{\delta bh^3}{4L^3} \quad (3.4)$$

In the equations, σ is the bending stress, M is moment about the neutral axis (caused from the applied load), y is the perpendicular distance to the neutral axis, I is the moment of inertia about the x -axis, ε is strain, δ is the measured deflection, b is the width of the beam, h is the thickness of the beam, and L is the length of the beam. The results showed that curing the specimens did not result in a substantial change in the modulus of elasticity, or a decrease in E if any change at all.

Property	ASTM	Units	Metric	Units	Imperial
Tensile Strength	D-638-03	MPa	50-60	psi	7,250-8,700
Elongation at Break	D-638-05	%	15-25	%	15-25
Modulus of Elasticity	D-638-04	MPa	2,000-3,000	psi	290,000-435,000
Flexural Strength	D-790-03	MPa	60-70	psi	8,700-10,200
Flexural Modulus	D-790-04	MPa	1,900-2,500	psi	265,000-365,000
HDT, oC @ 0.45MPa	D-648-06	oC	45-50	oF	113-122
HDT, oC @ 1.82MPa	D-648-07	oC	45-50	oF	113-122
Izod Notched Impact	D-256-06	J/m	20-30	ft lb/inch	0.375-0.562
Water Absorption	D-570-98 24hr	%	1.5-2.2	%	1.15-2.2
Tg	DMA, E>>	oC	48-50	oF	118-122
Shore Hardness (D)	Scale D	Scale D	83-86	Scale D	83-86
Rockwell Hardness	Scale M	Scale M	73-76	Scale M	73-76
Polymerized Density	ASTM D792	g/cm3	1.18-1.19		
Ash Content	USP281	%	0.21-0.22	%	0.21-0.22

Figure 3.5. VeroBlue material properties [28]

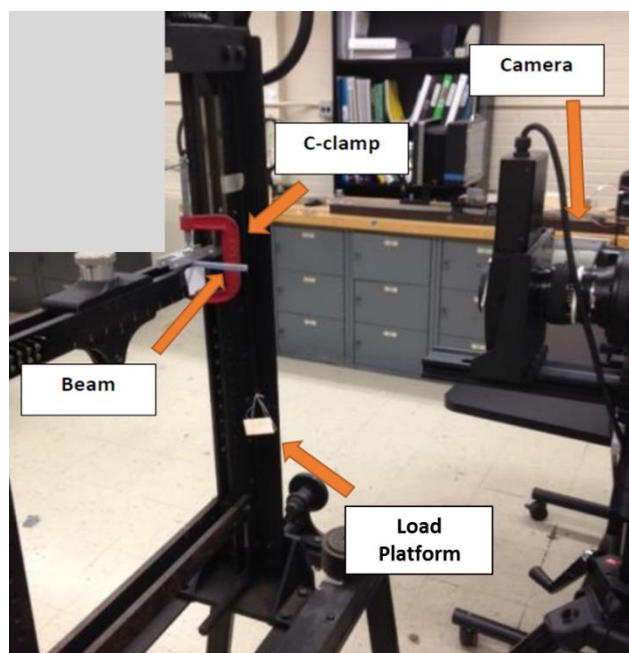


Figure 3.6. Bending cantilever beam test setup

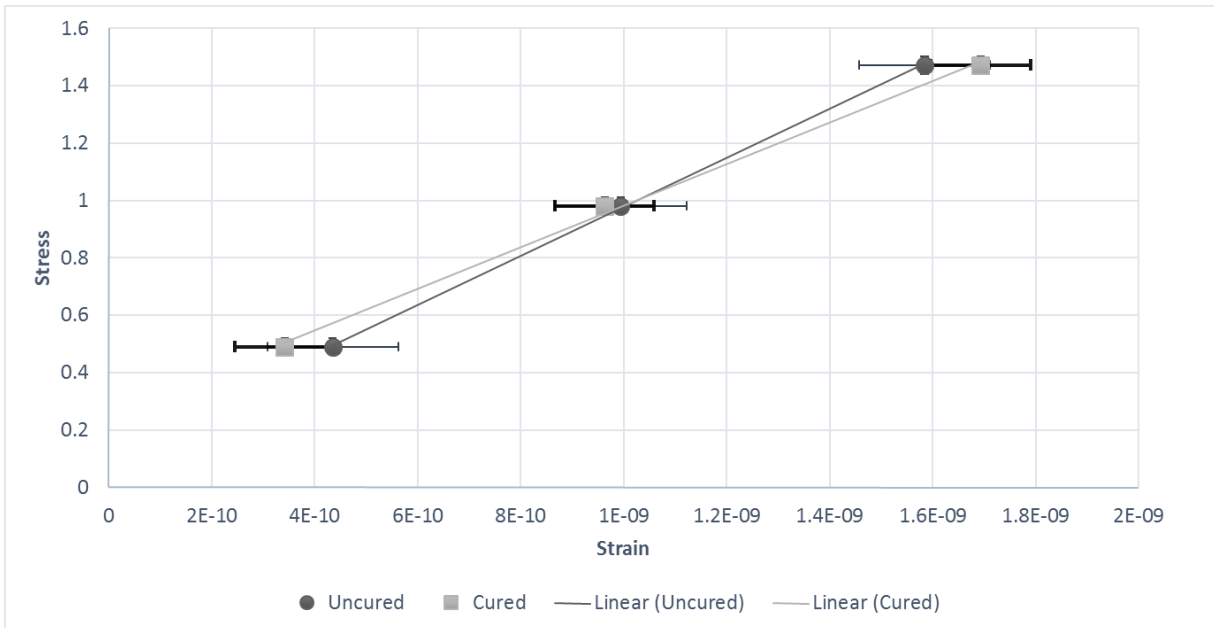


Figure 3.7. Bending beam test results

The Stratasys Dimension SST 1200es is also a commercial grade 3D printer. It uses fused deposition modeling to create parts from *ABSplus* plastic material. It prints with a layer thickness of 0.01 in with a build size of up to 10 x 10 x 12 in (254 x 254 x 305 mm). The support material is composed of Soluble (SST 1200es) and Breakaway (BST 1200es). This printer was used to create molds for the membrane adhering process, discussed in section 3.2.



Figure 3.8. Stratasys Dimension SST 1200es 3D printer

3.2 TEST ARTICLES

The Objet30 Pro 3D printer was used for printing the frames. The frames were designed in SolidWorks. The printed frames are 6.0 in x 3.0 in x 0.11 in (152 mm x 76 mm x 2.8 mm), creating an aspect ratio of two. The battens are each 0.15 in (3.8 mm) wide. A top view of the frame without the membrane is shown in Fig. 3.9.

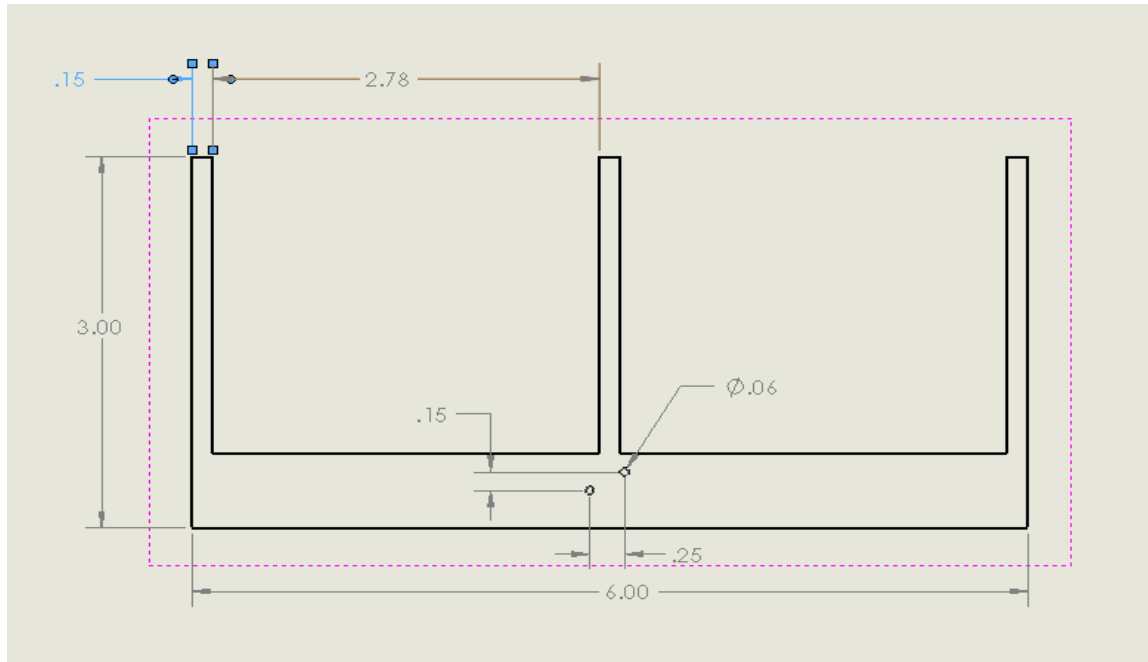


Figure 3.9. Top view of frames without membrane. Dimensions are in inches

The aspect ratio of 2 was chosen based on previous studies of low aspect ratio specimens [12-14]. Additionally, the cell AR \sim 1 and 2-cell frames were selected because Zhang *et al.* [12] found these characteristics to be optimal in terms of membrane effects on aerodynamic characteristics in previous tests. Frames with 2%, 4%, and 6% camber were printed following the NACA 4-series specification, as well as frames with no camber. Frames also vary in thickness and maximum camber location. A frame with a NACA 4504 (4% max camber, 50% max camber location, and 4% thickness) airfoil is shown in Figure 3.10. A table of test specimens is shown below.

Table 3.1. Test Specimens

NACA Designation	Max camber (%)	Max camber location	Thickness (%)
2504	2	0.5c	4
4504	4	0.5c	4
6504	6	0.5c	4
4506	4	0.5c	6
4404	4	0.4c	4
4604	4	0.6c	4

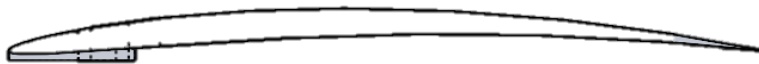


Figure 3.10. Top: 3D-printed NACA 4504 frame for a membrane MAV wing. Bottom: Cross-section for 3D-printed frame

The membrane adhered to the frames is a silicone rubber material with a thickness of $.010 \pm 0.002$ in (0.025 ± 0.005 cm), a tensile strength of 800 psi (5.52 MPa), and a hardness of 20 A¹. The modulus for the membrane is significantly lower than the modulus of the frame; hence, the flexibility in the wing is derived from the membrane. An adhesive called Dragon Skin was used to adhere the silicone membranes to the frames. Adhering silicone membranes with Dragon Skin followed a process developed by Abudaram *et al.* [17]. For the adhering process, frame molds were 3D printed for each frame using the Stratasys Dimension SST from Figure 3.8. The membrane was placed on the mold, followed by the frame with applied dragon skin and a weighted object as shown in Figure 3.12. Each membrane was then cut to form a trailing edge scallop of 25% of the membrane chord, a means to reduce drag but maintain lift [15]. Frames were printed with airfoils (battens) of 2504, 4504, and 6504 (Figure 3.12). Additionally, a flat frame was printed for comparison. Figure 3.13 shows the printed test subjects.

¹ As reported by the manufacturer.

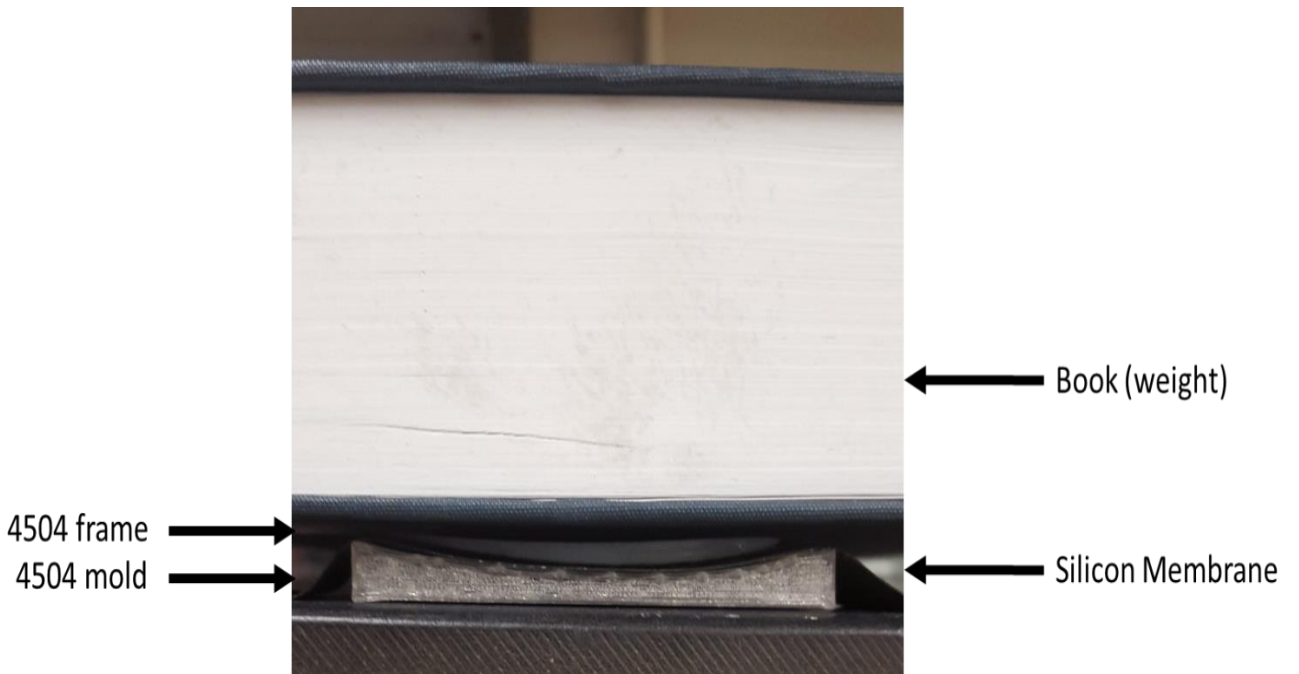


Figure 3.11. Top view (top) and side view (bottom) of attaching the membrane to a NACA

4504 frame

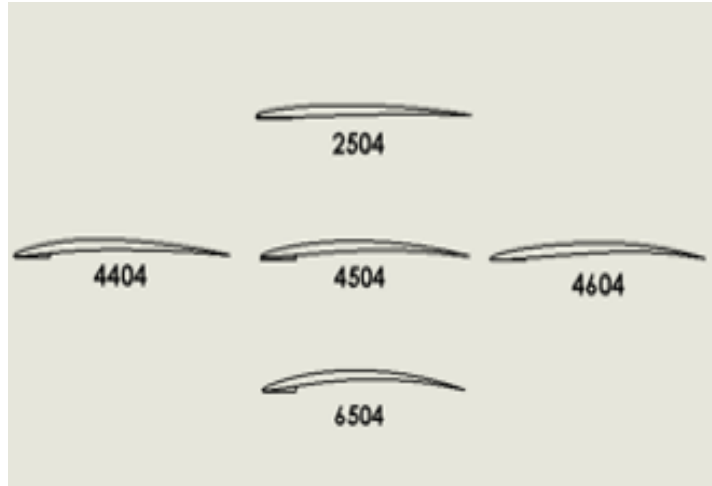


Figure3.12. NACA-designated airfoils tested



Figure 3.13. Test articles

3.3 DATA ACQUISITION

A Nano-17E ATI Industrial Automation load cell was used to measure forces and moments in the x , y , and z directions. The load cell has a resolution of 1.41×10^{-3} lb (6.25×10^{-3} N) for force measurements and 2.5×10^{-4} lb·in (3.13×10^{-2} N·mm) for moment measurements. This corresponds to a force and moment coefficient resolution of 0.009 and 5×10^{-5} , respectively, for the test conditions. To calibrate the load cell for force measurements, a first order, 6x6 matrix (Eq. 3.5) was used for the conversion of voltage to forces and moments.

$$\begin{bmatrix} F_x \\ F_y \\ F_z \\ M_x \\ M_y \\ M_z \end{bmatrix} = \begin{pmatrix} a_{11} & \cdots & a_{16} \\ \vdots & \ddots & \vdots \\ a_{61} & \cdots & a_{66} \end{pmatrix} \begin{bmatrix} V_1 \\ V_2 \\ V_3 \\ V_4 \\ V_5 \\ V_6 \end{bmatrix} \quad (3.5)$$

Angle-of-attack setting was achieved using a Velmex Xslide XN10-0120-E25-21 linear traverse to control a traversing arm with a range of -4 to 24° as shown in Figure 3.14. The mounting device has a low profile design to minimize the effect from horseshoe vortices

A schematic detailing the LabVIEW program, “Acquire Lift and Drag.vi”, used for acquiring force measurements for a range of angles-of-attack is shown in Figure 3.15. First, pressures and temperatures are recorded to determine the dynamic pressure, calculated from the “Tunnel Speed Record.vi” sub-VI. Load cell output is then read through the National Instruments SCXI 1000 system composed of a front mounted SCXI 1314, strain gage input SCXI 1520, and a 16-bit USB DAQ module SCXI 1600. After forces and moments are gathered at a set

angle-of-attack, the “MAV AOA Traverse Controller.vi” sub-VI commands the step motor controller to move the linear traverse, consequently adjusting the pitching mechanism to the new angle-of-attack.

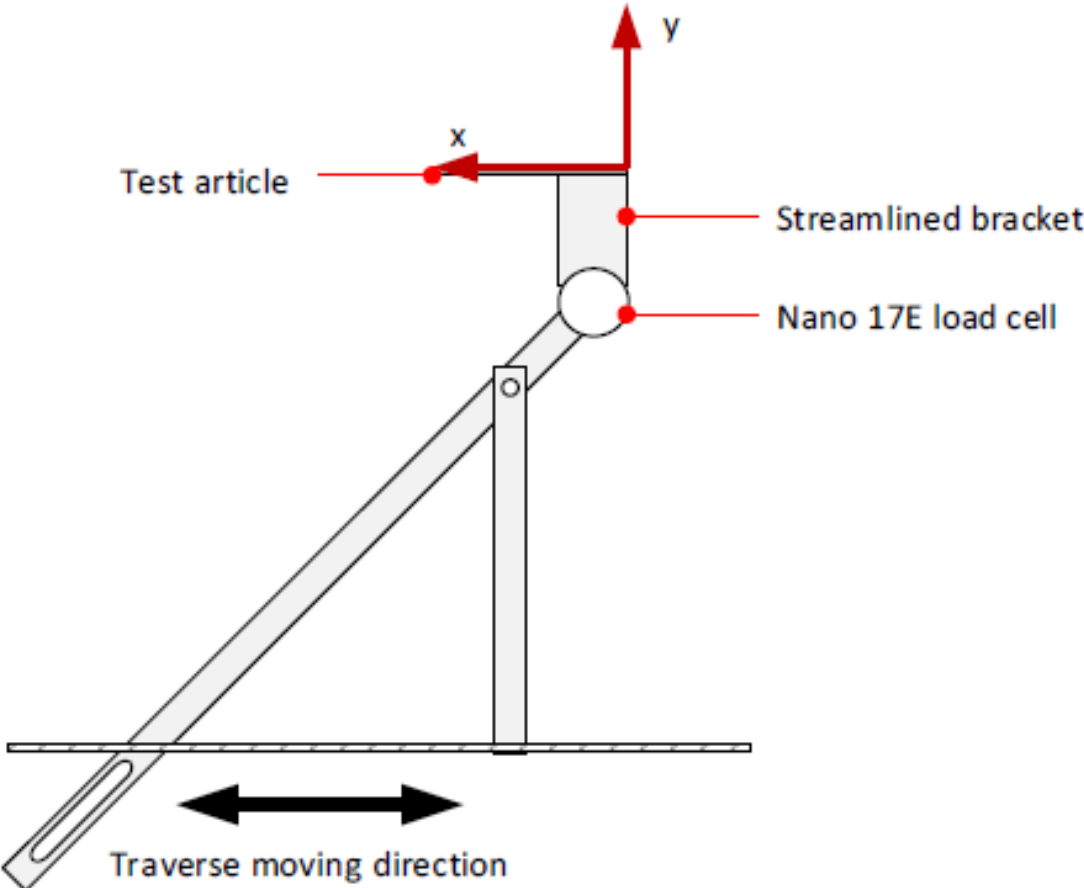


Figure 3.14. Test article/traverse setup in wind tunnel coordinate system [12]

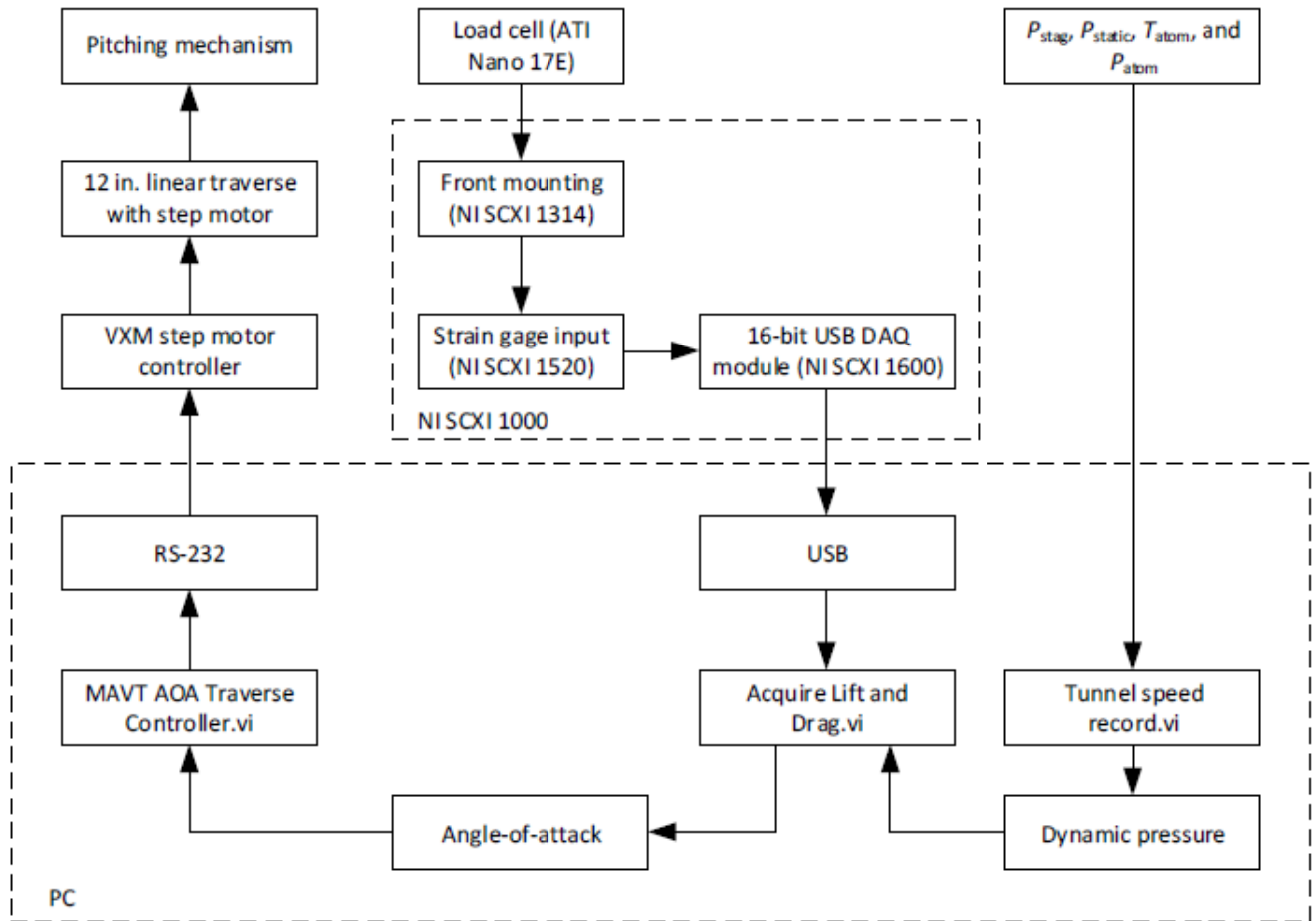


Figure 3.15. Load cell DAQ system for aerodynamic force measurement [12]

Using the load cell force and moment measurements (rotating body-axis system), lift, drag, and pitching moment coefficients (wind-axis system) were calculated for the experimental tests. Within the program, subVIs “MAVT AOA Traverse Controller.vi” and “Tunnel Speed Record.vi” is called for controlling the angle-of-attack and recording the tunnel speed for calculations. Before each test, the offset angle of the load cell, shown in Figure 3.16, is determined from a wind-off test. The offset angle is the angle between the load cell axis system and the free stream flow when the model is set at zero angle of attack. The offset angle

determination process is detailed in Fig. 3.17. The resulting forces were then imported into a MATLAB program, located Appendix A.1, for offset load cell angle calculation.

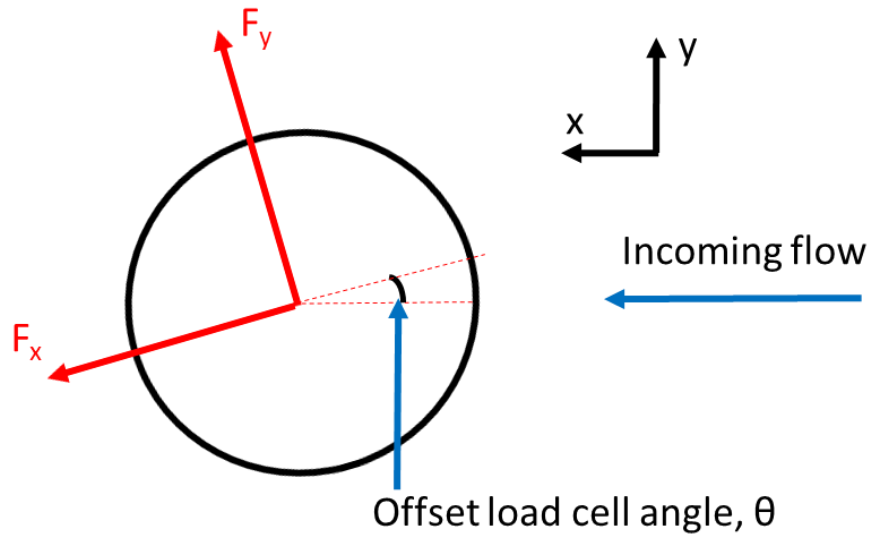


Figure 3.16. Offset load cell angle when the model is set to zero angle of attack

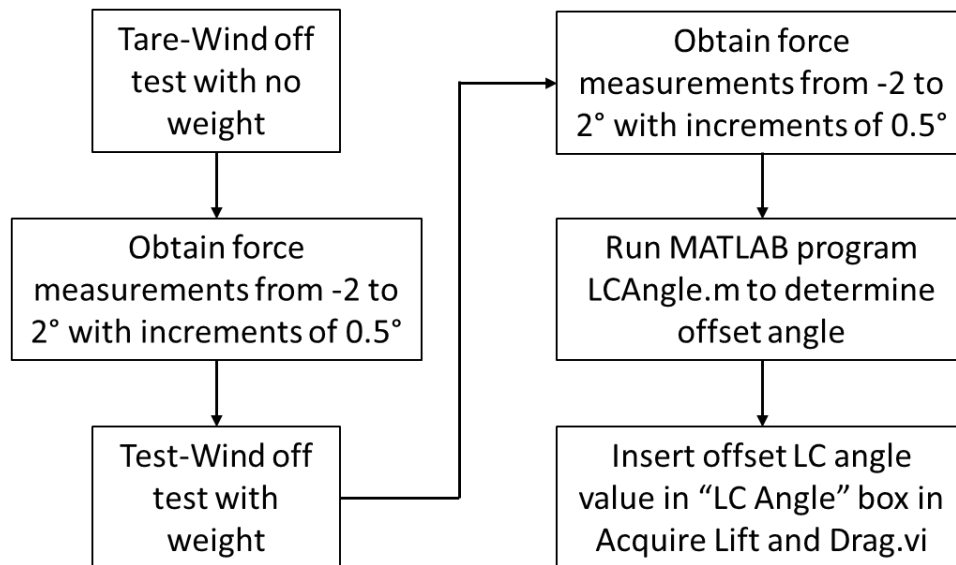


Figure 3.17. Load cell offset angle calculation

Subsequently, the experiment was conducted—first with wind off (a tare run to account for the changing position of the model during the angle of attack sweep) and a second run-through with wind on to acquire the aerodynamic forces. After acquiring the forces for each angle-of-attack and subtracting the tare loads, lift and drag forces were calculated using the following equations:

$$\alpha' = \alpha + \theta \quad (3.6)$$

$$L = F_y \cos(\alpha') - F_x \sin(\alpha') \quad (3.7)$$

$$D = F_y \sin(\alpha') + F_x \cos(\alpha') \quad (3.8)$$

Note that α' in the equations above is the angle-of-attack corrected for wind tunnel angle and offset load cell angle. The MATLAB program in Appendix A.1 was used for calculating the offset load cell angle, θ , which is positive in the counter-clockwise direction of Fig. 3.16. The flow chart below gives a general overview of the data acquisition process for the LabVIEW program that acquired lift and drag for the range of angles-of-attack. Additionally, the front panel for the program is shown in Fig. 3.19.

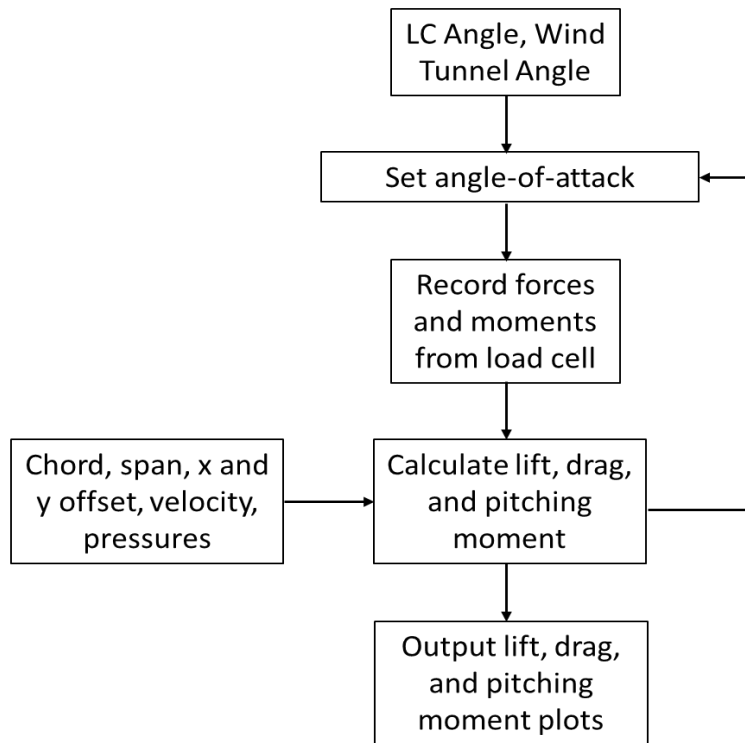


Figure 3.18. Process for aerodynamic coefficient plot generation using Acquire Lift and Drag.vi

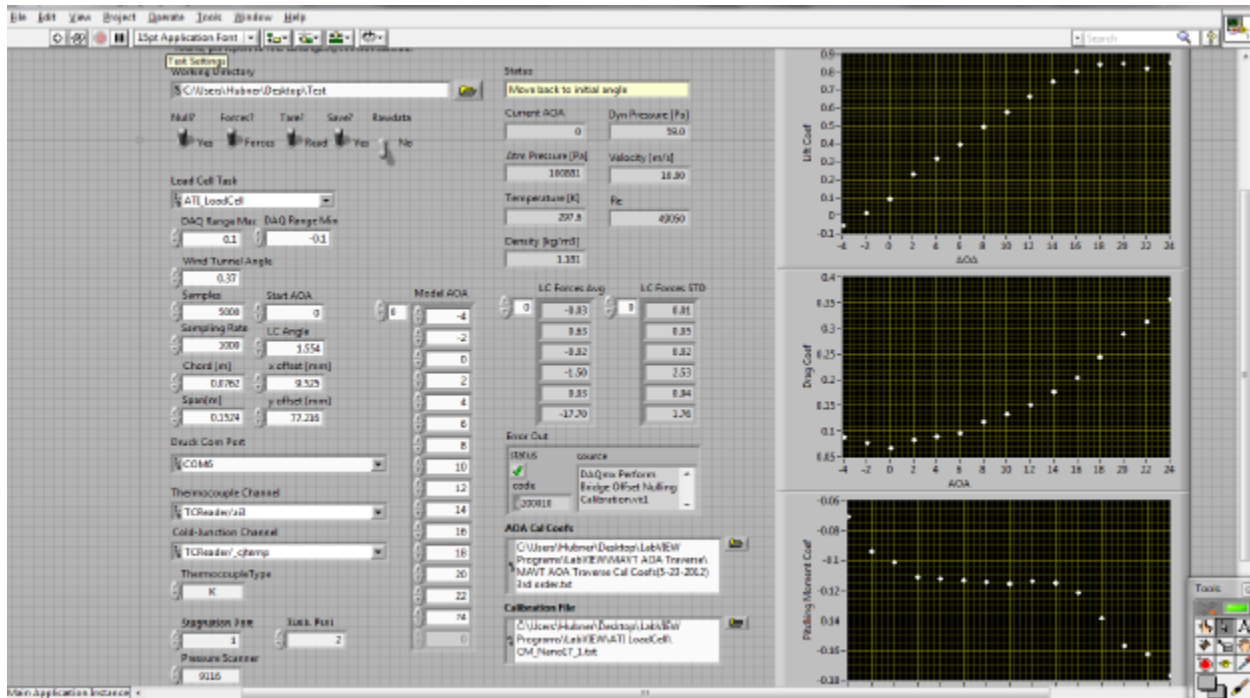


Figure 3.19. Front panel of Acquire Lift and Drag.vi

3.4 Digital Image Correlation

A Correlated Solutions' VIC-3D System was borrowed from Dr. Jialai Wang of the Civil Engineering Department for digital image correlation (DIC) measurements of the membrane deformation. The DIC system used a dual-camera configuration with the line of sight for both cameras angled at 90° from each other and normal to the flow. Figure 3.20 shows a top view of the DIC system setup with respect to the wind tunnel and test articles.

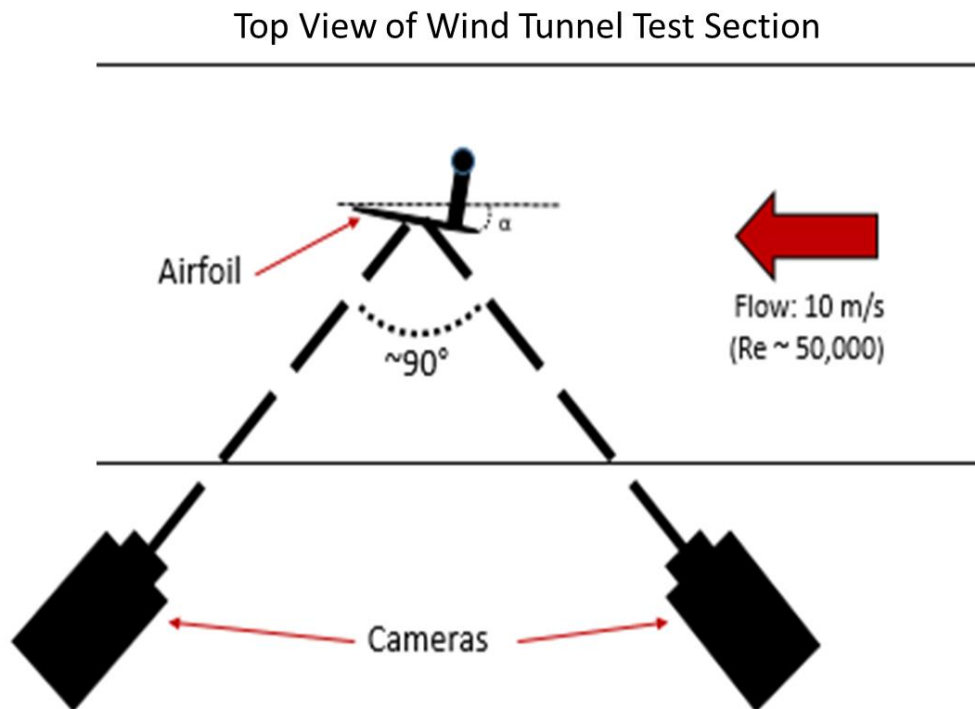


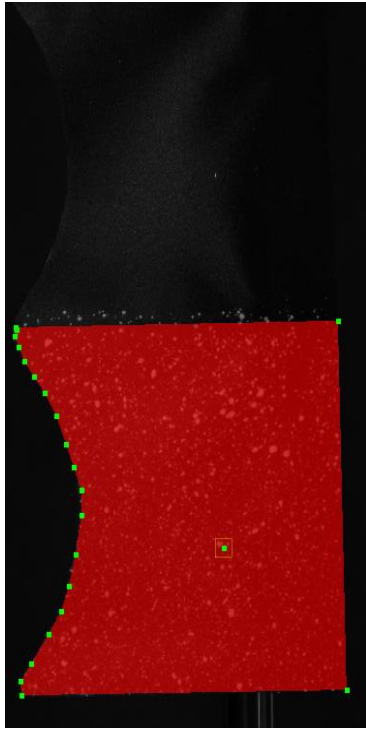
Figure 3.20. DIC system setup

Approximately 100 images were acquired during each test with an exposure time of 1 ms. Correlated Solution's software was used for developing displacement matrices for the vibrating membranes. The system is quoted to have the capability of measuring arbitrary

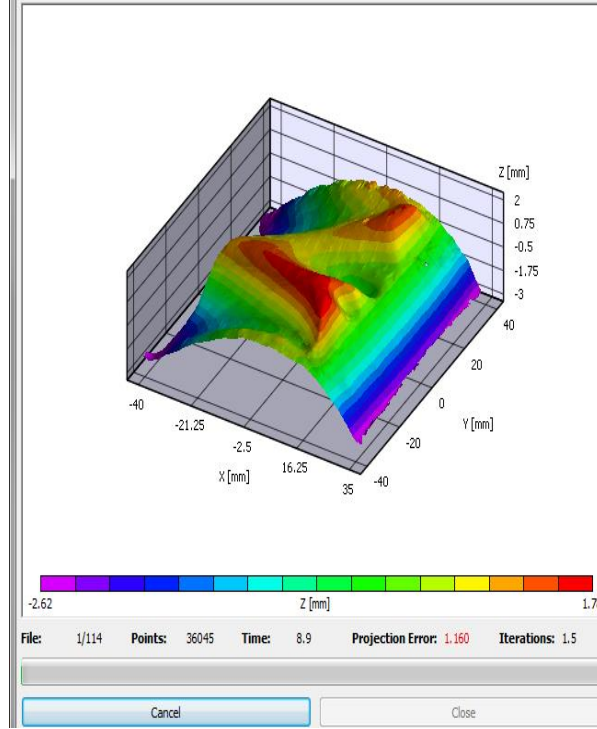
displacements of 0.05 mm for specimen sizes ranging from less than 1 mm to greater than 10 m. For the software to measure displacement, a random speckle pattern is applied to the membrane surface as shown in Figure 3.21. The speckle pattern was generated using white spray paint. Only half of the wing was painted to improve the field-of-view and corresponding resolution (symmetry was assumed). The software allows for the designation of a specific section geometry for displacement analysis. When this section is selected, displacement plots for each of the acquired images are generated as shown in Fig. 3.22. For the DIC tests, the wings were oriented at 6° and 18° angles-of-attack. Those angles were chosen as they represent the regions of peak aerodynamic efficiency and high (near maximum) lift coefficient, respectively. Further post-processing of the data, including data smoothing, aerodynamic twist measurements, and lifting-line theory calculations will be presented in Chapter 4.



Figure 3.21. Spray-painted speckle pattern on upper surface of wing



(a)



(b)

Figure 3.22. Correlated Solutions displacement analysis software. (a) is the geometry selection procedure, while (b) is the displacement plot output

CHAPTER 4. RESULTS AND DISCUSSION

4.1 Introduction

This chapter presents the experimental and theoretical results for flexible membrane wings with cambered, 3D printed frames. The wings were tested at a Reynolds number of 50,000 (10 m/s) while varying angles-of-attack from -4 to 24° . The results, including lift, drag, and pitching moment coefficients, for the experimental investigation are presented in section 4.2. While it neglects the effects of viscosity and is generally limited to high aspect ratio wings and high Reynolds number flows, lifting-line theory (LLT) was used to perform a theoretical analysis on the time-averaged shapes for the membrane wings because of its effectiveness for predicting lift and induced drag for wings with varying geometric twist and chord lengths. The basic theory of LLT is presented in Section 4.3. The calculated values were compared with the experimental values to determine the effectiveness of using the theory for approximating time-averaged aerodynamic coefficients. Section 4.3 discusses the acquisition and analyses of the time-averaged shapes.

4.2 Experimental Force and Moment Measurements

Three separate tests were performed for each wing. Repeated tests were performed on different days. Figures 4.1-4.9 represent the median curves for each model. The median curves were chosen due to the presence of outliers in a few tests.

4.2.1 Varying Maximum Camber

Figures 4.1-4.3 show the effects of changing maximum camber on aerodynamic forces and moments. As mentioned in Chapter 3, the uncertainties for the force and moment coefficients are 0.009 and 5×10^{-5} , respectively. In the legends for the plots, the first number represents the maximum camber as a percentage. For example, 4504 indicates a maximum camber of 4%. The error bars in the figures are based on the aforementioned uncertainties. From Figure 4.1, it is observed that wings with cambered frames exhibit lift advantages of up to 16%, especially at higher angles-of-attack in the stall region when compared to those with flat frames. For lower angles-of-attack, drag reductions of up to 40% (at $\alpha = 6^\circ$) were measured with cambered frames, with the exception of 6% camber frame which produces similar drag to wings with flat frames. At higher angles-of-attack, the 2504 and 4504 frames experienced drag reductions of 10-20% when compared to flat frames, while the 6504 frame experienced similar to slightly higher drag. Increasing frame camber increases lift, particularly at high angle-of-attack with the 6% cambered frames outperforming the rest of the wings. This corresponds to an expected shift to the left and up of the lift curve due to cambering.

The L/D ratios, Figure 4.2, for each of the wings with cambered frames outperformed those of the flat frames by up to 60% with the maximum L/D ratios occurring between 6-12°. The ratio $C_L^{3/2}/C_D$ [19] was also compared, providing an indication of endurance efficiency for a propeller driven vehicle, as most fixed-wing MAVs use a propeller for propulsion. The wings with cambered frames of 6% experience the greatest endurance efficiency at 12°. This is a

result of the increased sensitivity with respect to lift. The wings with cambered frames of 2% and 4% camber also outperform the flat frames in endurance by up to 60% at $\alpha = 12^\circ$ and over 200% at $\alpha = 2^\circ$.

Figure 4.3 shows that the quarter-chord pitching moments for the wings with cambered frames are more negative than the flat frames, and increasing the frame camber creates a more negative moment. This indicates that the center of pressure of the cambered frames is behind the quarter chord. The pitching moment for the cambered frames stays relatively level for lower angles-of-attack and begins to decrease as the stall region is approached. Thus, the quarter-chord for low angles of attack is close to the aerodynamic center for the cambered frames. The decrease in pitching moment in the stall region is more prevalent as camber decreases. The flat frame displays a constant, negative slope instead of any level region. The C_m trend is likely due to angle-dependent cambering associated with frames of varying camber. The aerodynamic center for the flat frame membrane wing is aft of the quarter-chord.

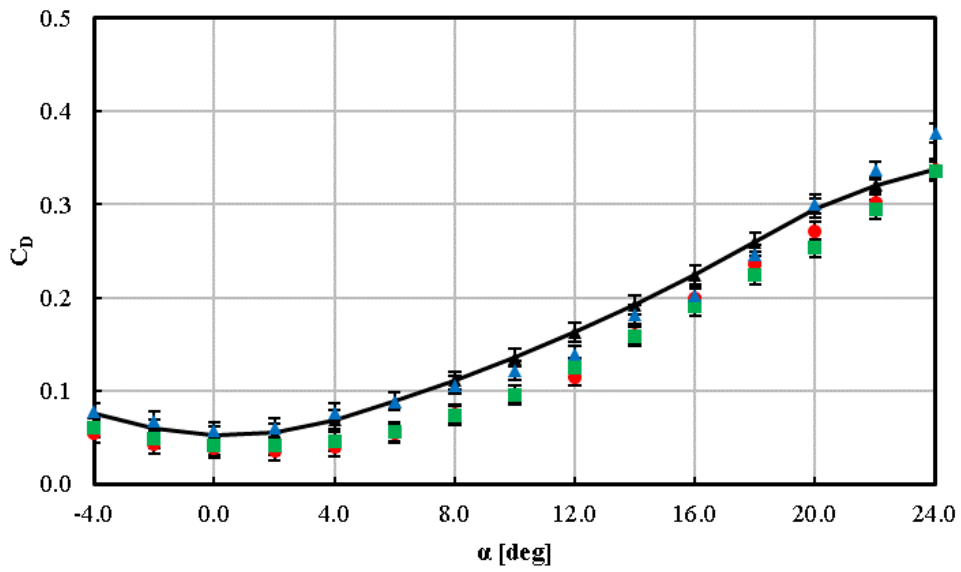
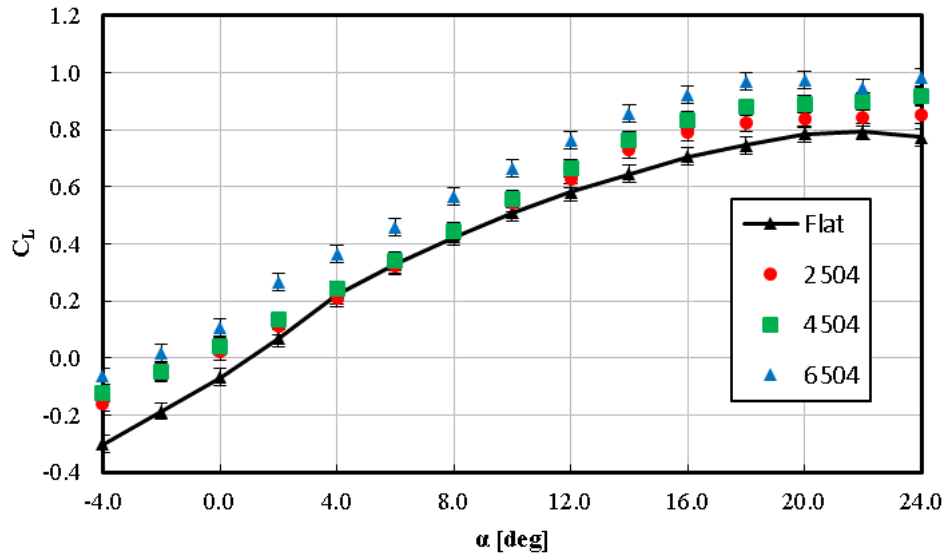


Figure 4.1. Plots for C_L and C_D with varying frame camber

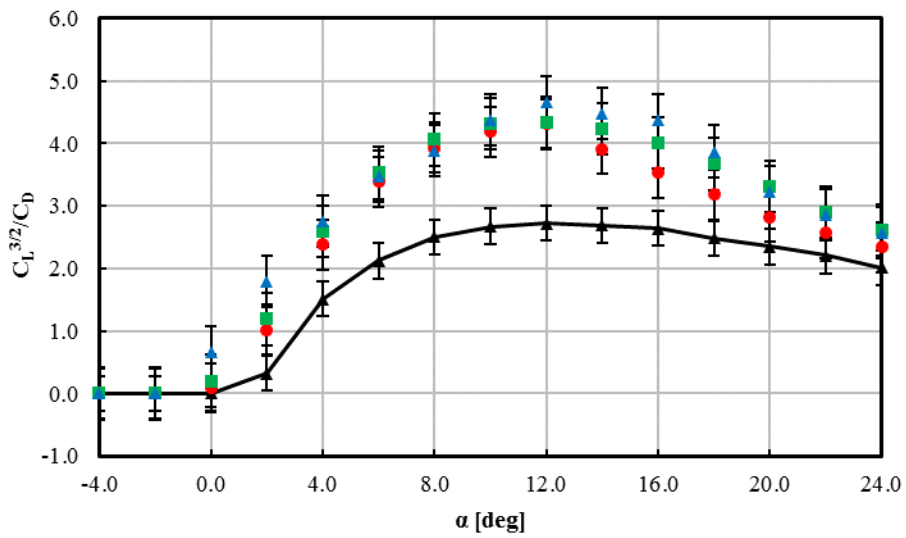
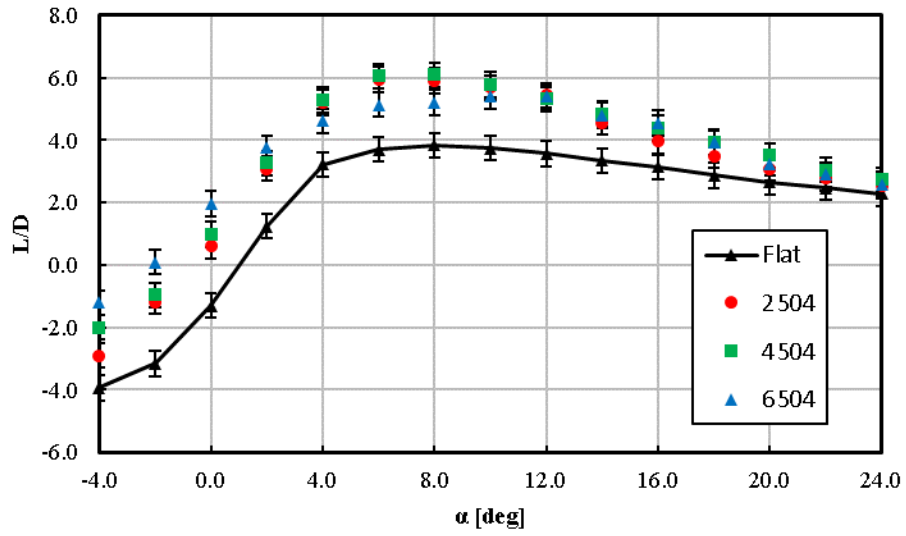


Figure 4.2. Plots for L/D and $C_L^{3/2}/C_D$ with varying frame camber

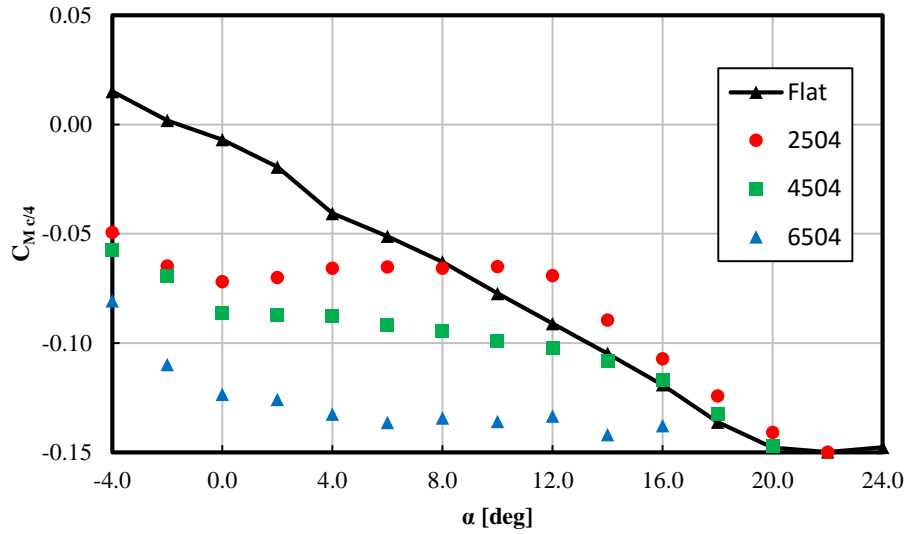


Figure 4.3. Plot for $C_M c/4$ with varying frame camber

4.2.2 Varying Maximum Camber Location

Figures 4.4-4.6 show the plots for the case when maximum camber location on the frame is adjusted upstream or downstream. In the legends for the plots below, the second number represents the location of the maximum camber as a percentage of chord length measured from the leading edge. For example, 4504 indicates a maximum camber located at 50% of the chord length. Similar to section 4.2.1, these cambered frames also outperformed the flat frames. While little difference (within uncertainty range) is observed in aerodynamic coefficient plots in Figure 4.4, the lift-sensitive endurance plot in Figure 4.5 displays a decrease in endurance when the maximum camber location is shifted fore or aft of $0.5c$.

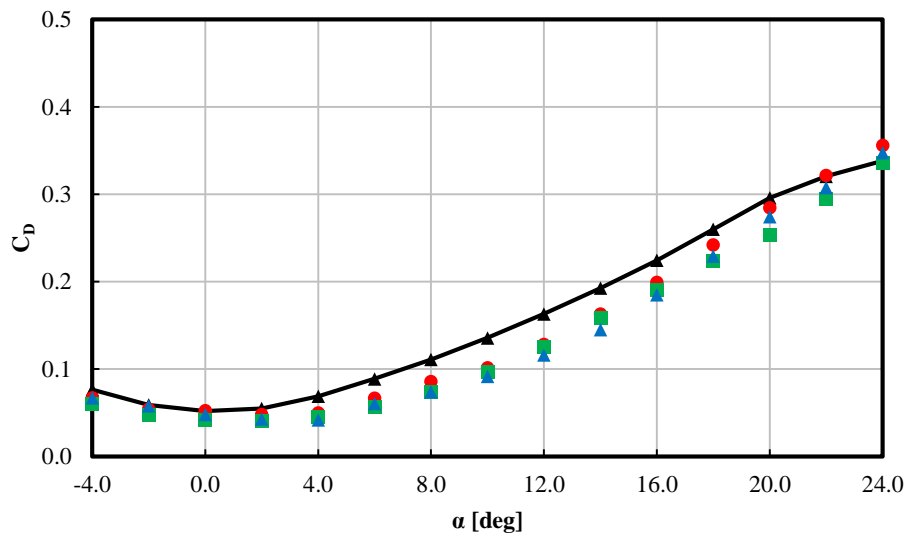
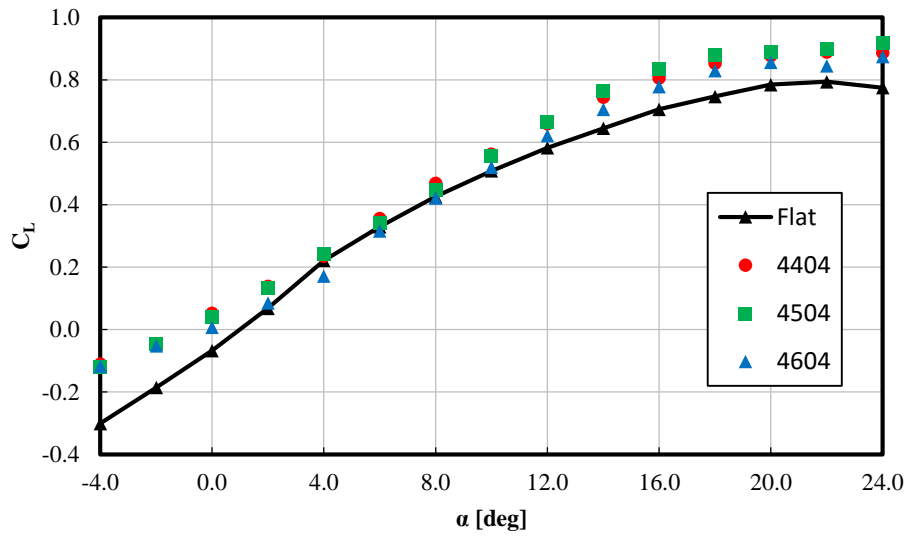


Figure 4.4. Plots for C_L and C_D with varying maximum camber location on frame

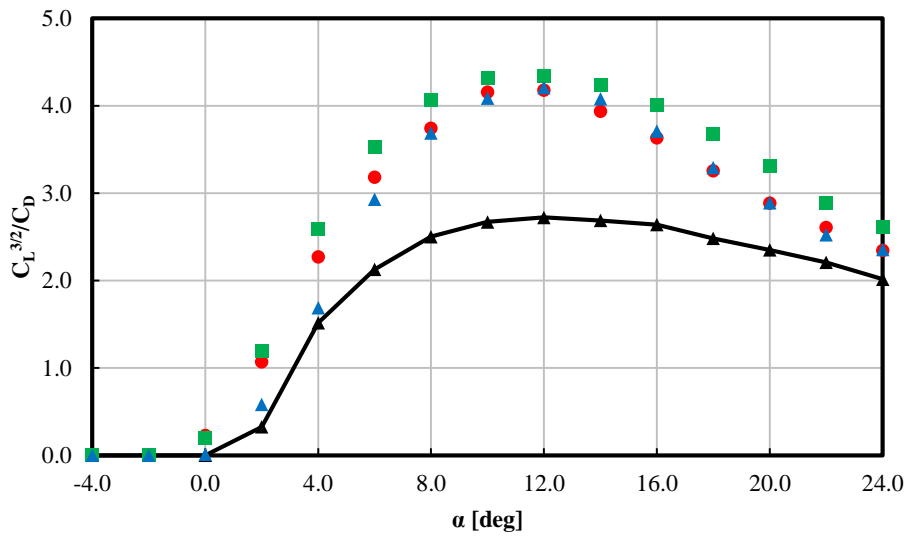
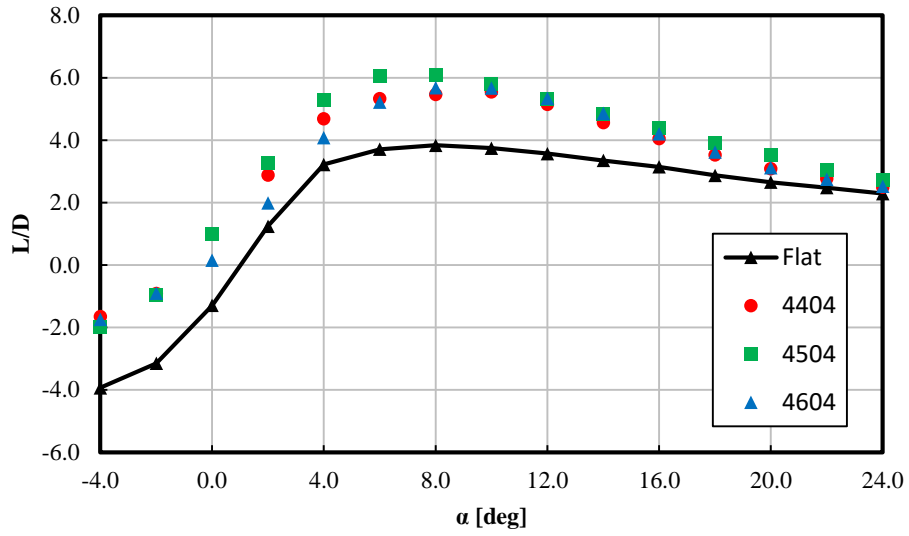


Figure 4.5. Plots for L/D and $C_L^{3/2}/C_D$ with varying maximum camber location on frame

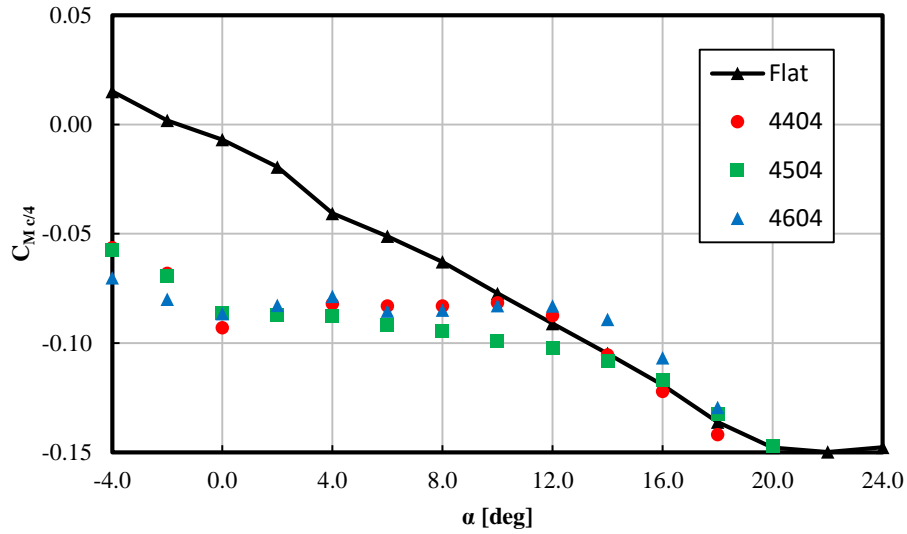


Figure 4.6. Plot for $C_M c/4$ with varying maximum camber location on frame

4.2.3 Varying Frame Thickness

Figures 4.7-4.9 show the resulting plots for the case when thickness is changed. In the legends for the plots below, the third and fourth numbers represent the thickness of the airfoil as a percentage of the chord. For example, 4504 indicates a frame thickness of 4%. Once again, the cambered frames showed better aerodynamic characteristics than the flat frames. However, Figure 4.8 shows that the cambered frame with a thickness of 6% had lower aerodynamic efficiency when compared with the cambered frame of 4% thickness. The cambered frame of 6% thickness only marginally increased lift, while increasing drag and decreasing L/D and endurance. One concern was whether frame flexibility could account for the measured differences between the 4% and 6% thickness frames. High-speed imaging of the

frames, though, showed negligible tip deflection differences (less than two pixels, corresponding to less than 0.10 in) between the two frames. The increased drag could be related to the increased projected frontal area or increased cavity size underneath the membrane and aft of the leading-edge region of the thicker 6% frame.

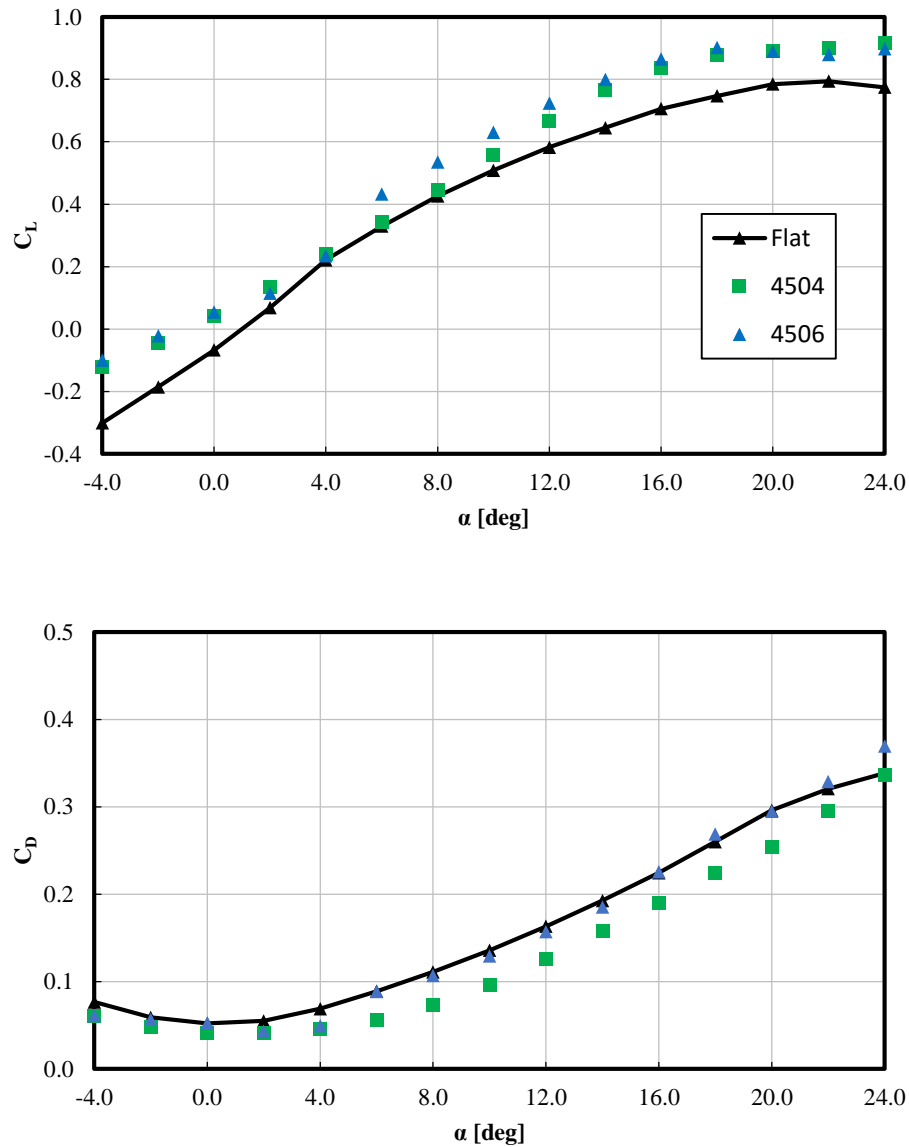


Figure 4.7. Plots for C_L and C_D with varying frame thickness

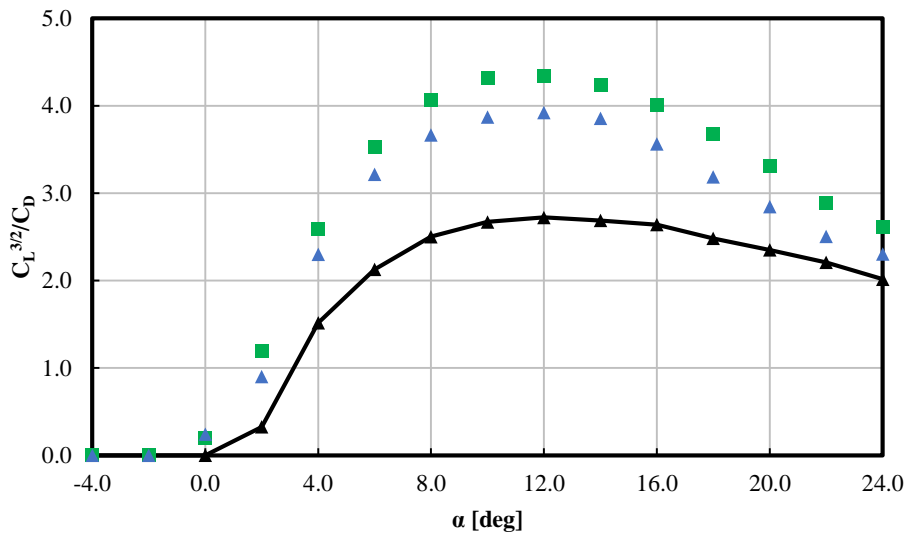
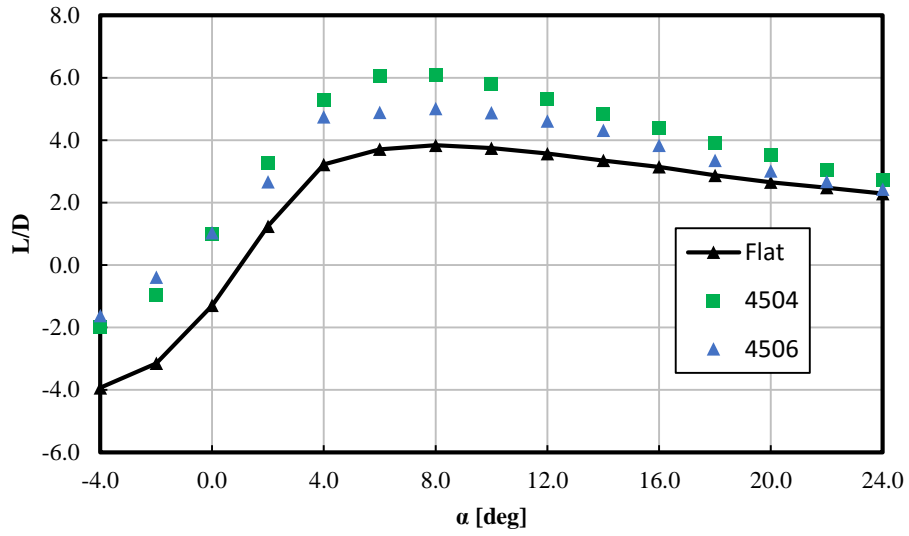


Figure 4.8. Plots for L/D and $C_L^{3/2}/C_D$ with varying frame thickness

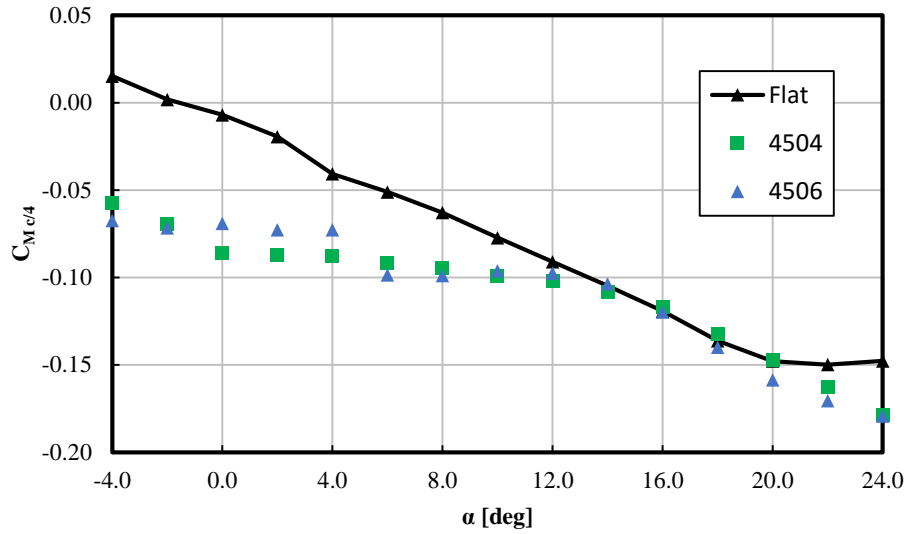


Figure 4.9. Plot for $C_M c/4$ with varying frame thickness

In summary, the aerodynamic force coefficients from the experimental study indicate that frame cambering had a larger effect than maximum camber location or frame thickness on the AR =2 membrane wings. Membrane wings with cambered frames displayed greater lift than those with flat frames by as much as 16%, particularly at angles-of-attack greater than 10°. Additionally, membrane wings with cambered frames produced less drag than those with flat frames with the exception of 6% cambered frame and 6% thickness. Therefore, aerodynamic efficiency and endurance measurements for the membrane wings with cambered frames were superior to those of the flat frames. From observing moment plots, increasing camber further decreased the pitching moment, and the aerodynamic center is near the quarter-chord for all cambered frames.

4.3 Time-Averaged Shape Theoretical Analysis

To better interpret and understand the force data, time-averaged shapes of the membrane wings were acquired. The time-averaged shapes were used as part of a lifting-line analysis to estimate lift and induced drag. The time-averaged shapes were acquired for specimens at 6° and 18°, corresponding to regions of high aerodynamic efficiency and approaching stall conditions, respectively.

As mentioned in Chapter 3, a DIC camera system was used for acquiring displacement matrices. The resulting displacement plots were averaged over time and used for a theoretical, lifting-line analysis. The lifting-line analysis used in this study is outlined by Bertin and Cummings [29]. Lifting-line theory considers effects from the local circulation, local chord length, local geometric angle of attack, and zero-lift angle-of-attack. Based on the Kutta-Joukowski theorem, the lift on an airfoil section of a wing is a function of the bound circulation. However, lift distribution, and hence spanwise circulation distribution, is not constant over a wing of finite span. Lifting-line theory represents the spanwise circulation distribution for a wing of finite span by the sine series in Equation 4.1.

$$\Gamma = \sum_1^n A_n \sin(n\phi) \quad (4.1)$$

Assuming wing symmetry about the centerline, only odd terms need to be retained. Figure 4.10 shows a hypothetical, symmetric spanwise lift distribution due to circulation where 0 and π represent the wingtips—points of zero circulation or lift. The first 4 sine terms are plotted,

along with their summation. The Matlab code developed for generating the plot is located in Appendix A.3.

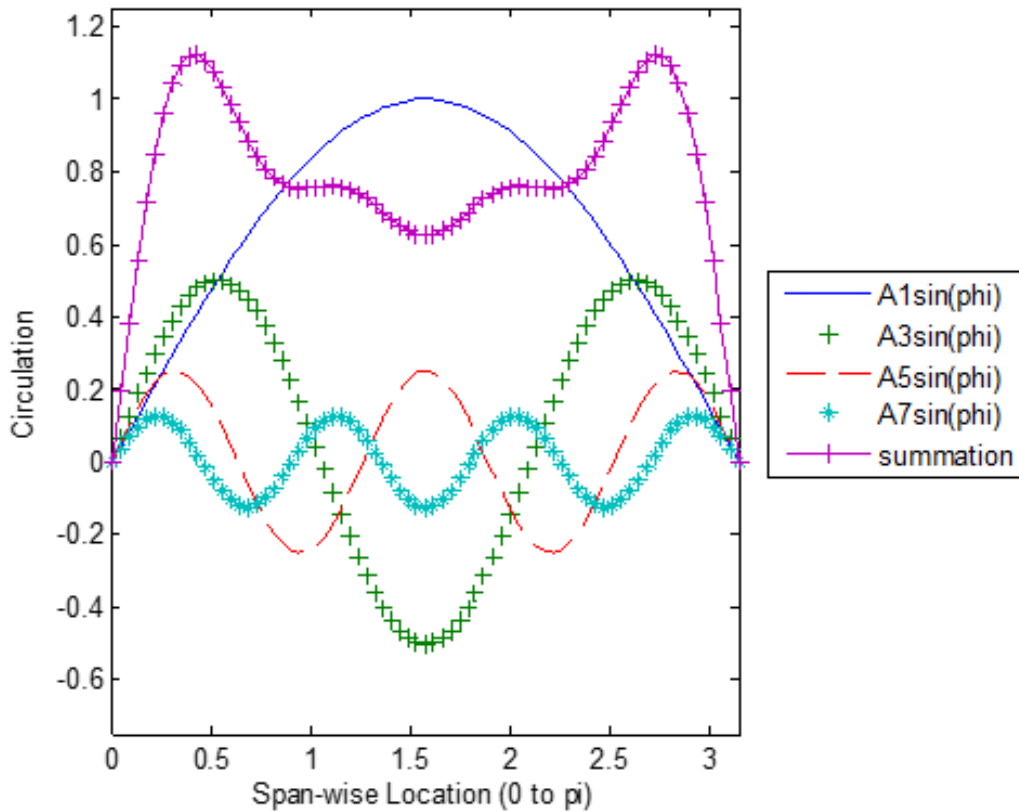


Figure 4.10. Example symmetric spanwise lift distribution for an unswept wing

In the applied lifting-line analysis, the following governing equation, known as the monoplane equation, was used:

$$\mu(\alpha - \alpha_{0l}) \sin(\phi) = \sum A_n \sin(n\phi) (\mu n + \sin(\phi)). \quad (4.2)$$

In Equation 4.2, $\mu = ca_0/4b$. Retaining the odd terms, results in Equation 4.3:

$$\begin{aligned} \mu(\alpha - \alpha_{0l}) \sin(\phi) = & A_1 \sin(\phi) (\mu + \sin(\phi)) + A_3 \sin(3\phi) (3\mu + \\ & \sin(\phi)) + A_5 \sin(5\phi) (5\mu + \sin(\phi)) + \dots \end{aligned} \quad (4.3)$$

Subsequently, a system of linear equations can be constructed for different ϕ values. Each ϕ value represents a different location along the span. The calculation for ϕ is shown in Eq. 4.4:

$$\phi = \cos^{-1} \left(-\frac{2y}{b} \right). \quad (4.4)$$

The number of A coefficients is the same as the number of spanwise locations used in the system of equations. When the system of equations is solved, A_1 is used to compute C_L as shown in Eq. 4.5 [29]:

$$C_L = A_1 \pi AR. \quad (4.5)$$

And, the induced drag is

$$C_{Dv} = \frac{C_L^2}{\pi AR} \left(1 + \frac{3A_3^2}{A_1^2} + \frac{5A_5^2}{A_1^2} + \dots \right). \quad (4.6)$$

An in-house MATLAB code used for the lifting-line theory analysis is located in Appendix A.2.

The basic structure of the code is detailed in Figure 4.11. First, the code imports the displacement matrices and converts each matrix into a format that is optimal for the analysis

process. The code analyzes the time-averaged shape and uses a third-degree polynomial approximation to reduce noise near the trailing edge, smoothing the chordwise, time-average displacements. Figure 4.12 illustrates typical results of the polynomial approximation process. In addition to the data smoothing function, a correction for the offset slope was applied. This correction was necessary due to slight displacement readings between the leading edge and trailing edge of the software.

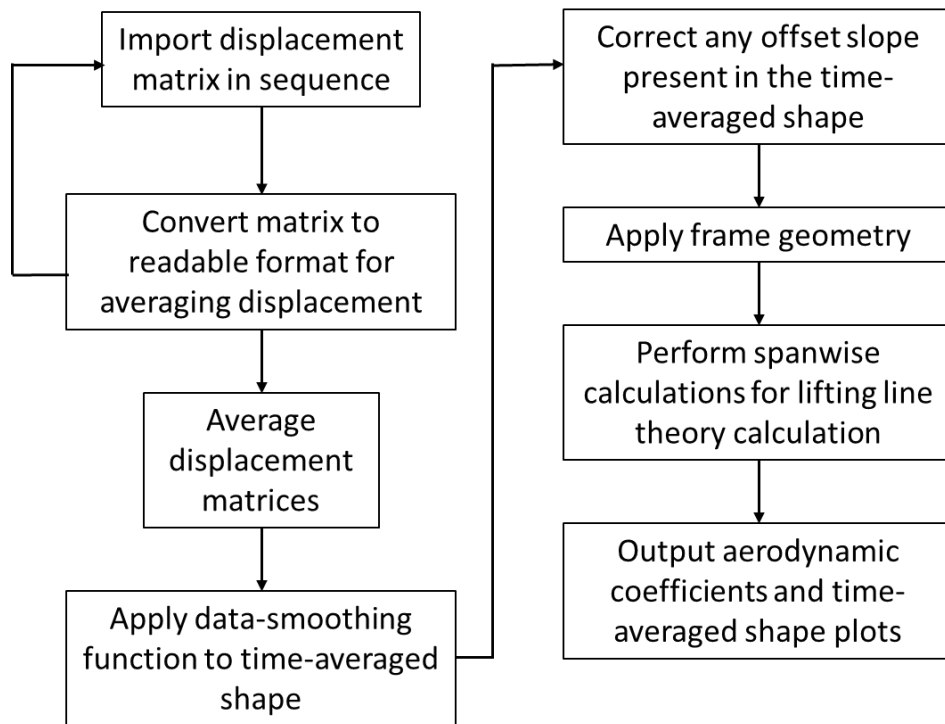


Figure 4.11. MATLAB code structure

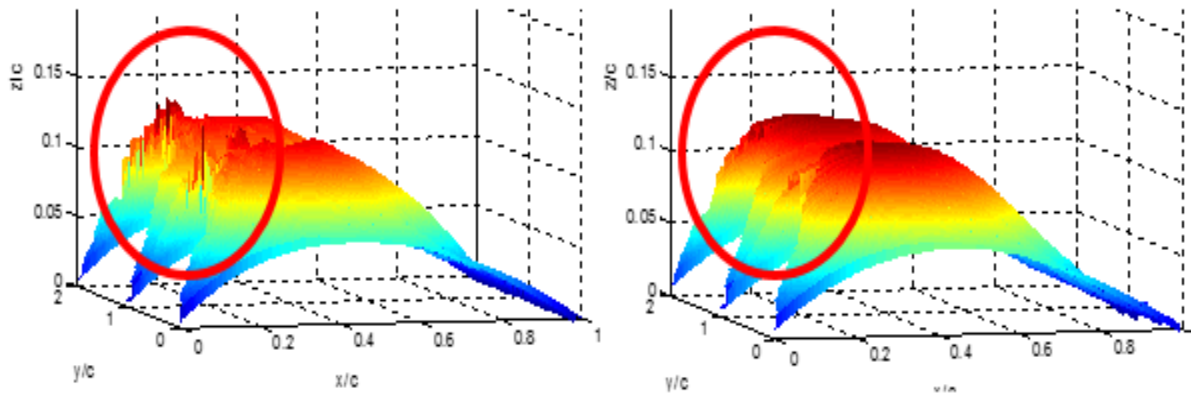


Figure 4.12. Effect of third degree polynomial fit on the trailing edge on the NACA 4504 frame

The code incorporated the monoplane equation to compute aerodynamic coefficients using 100 sections evenly spaced across the span, although results typically converged with less than 10 iterations. As ϕ changes with spanwise location, geometric twist (local airfoil twist relative to the root chord, due to membrane trailing-edge deflection) and aerodynamic twist (local airfoil zero-lift angle-of-attack, due to membrane cambering) changes due to the membrane deflection. The chord length is also spanwise dependent due to trailing-edge scalloping, as shown in Figure 4.13. As previously mentioned, this makes the monoplane equation ideal for the geometries produced by the time-averaged shapes. Figure 4.14 illustrates the flow chart for the section of the code employing the lifting-line analysis. In the time-averaged plots, note that the coordinate access has shifted from the wind tunnel coordinates to wing coordinates. For example, the leading edge is located at $x/c = 1$, and z/c refers to the out-of-plane displacement of the membrane wing.

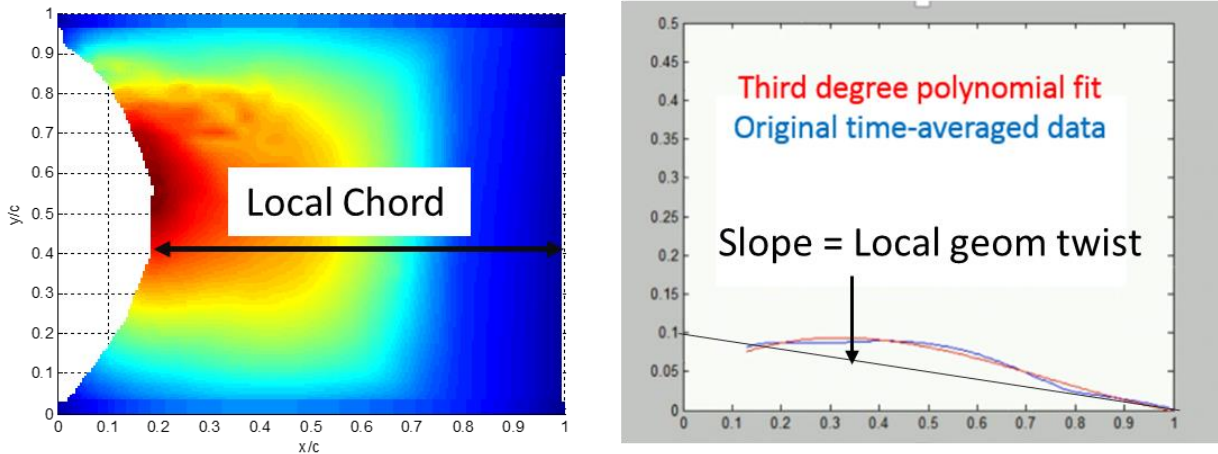


Figure 4.13. Local chord and effective angle-of-attack

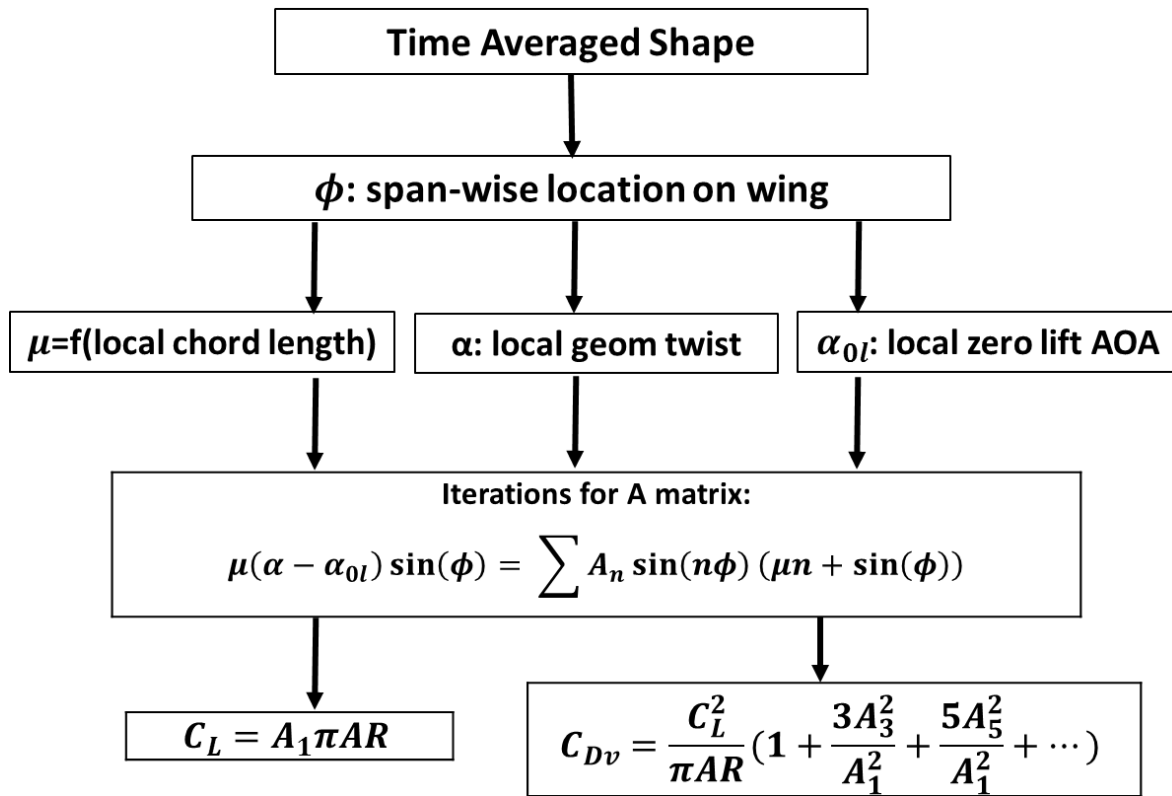


Figure 4.14. Lifting-line analysis flow chart

Figure 4.15 shows the theoretical and experimental results for the 2504, 4504, and 6504 at an angle-of-attack of 6° where the aerodynamic efficiency is high. With the exception of the membrane wing with 6504 frame, the theory reasonably approximates ($\sim 10\%$ lower) the lift coefficient at 6° angle-of-attack. From observing the time averaged shapes at this angle-of-attack in Figure 4.16, the membrane wing with the 6504 frame has noticeably more membrane displacement near the leading edge compared to the 2504 and 4504 wings, creating a region of substantial negative camber near the leading-edge.

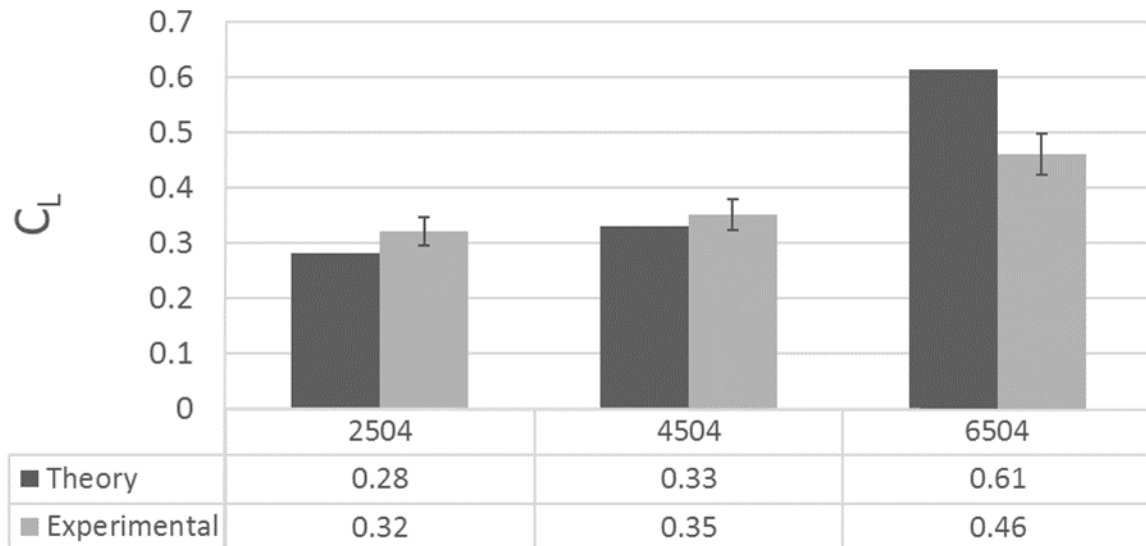


Figure 4.15. Lift coefficient at 6°

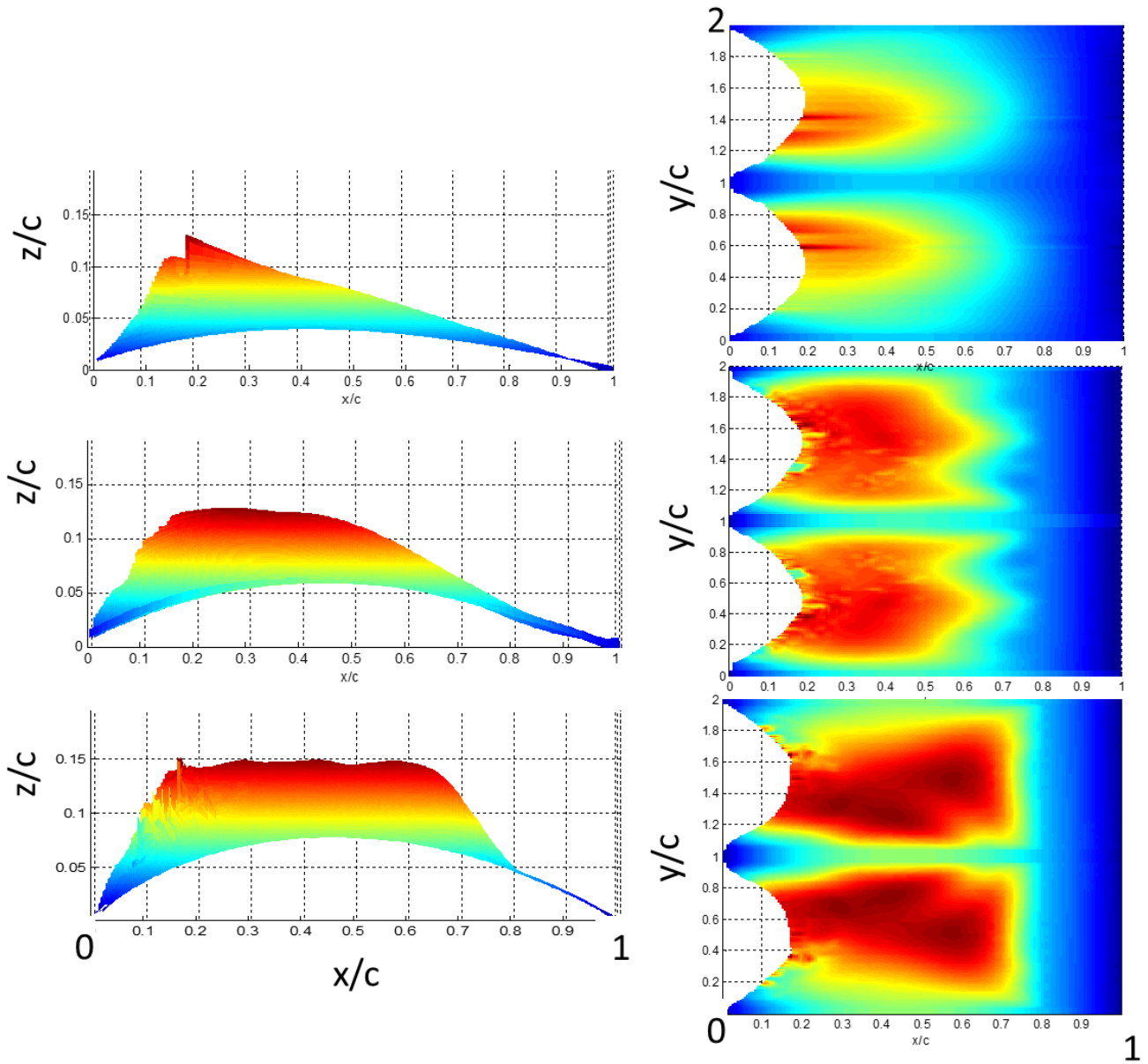


Figure 4.16. Time-averaged shapes at 6° (side view on left, top view on right). From top to bottom: 2504, 4504, 6504. Flow is from right to left. Red indicates more deflection, while blue indicates little to no deflection

The results at 18° near the maximum lift coefficient, shown in Figure 4.17, were similarly consistent between theory and experiment across all three wing cambers, with the largest difference of 5% over-prediction of the 6504 wing. Figure 4.18 displays the time-averaged shapes for this condition.

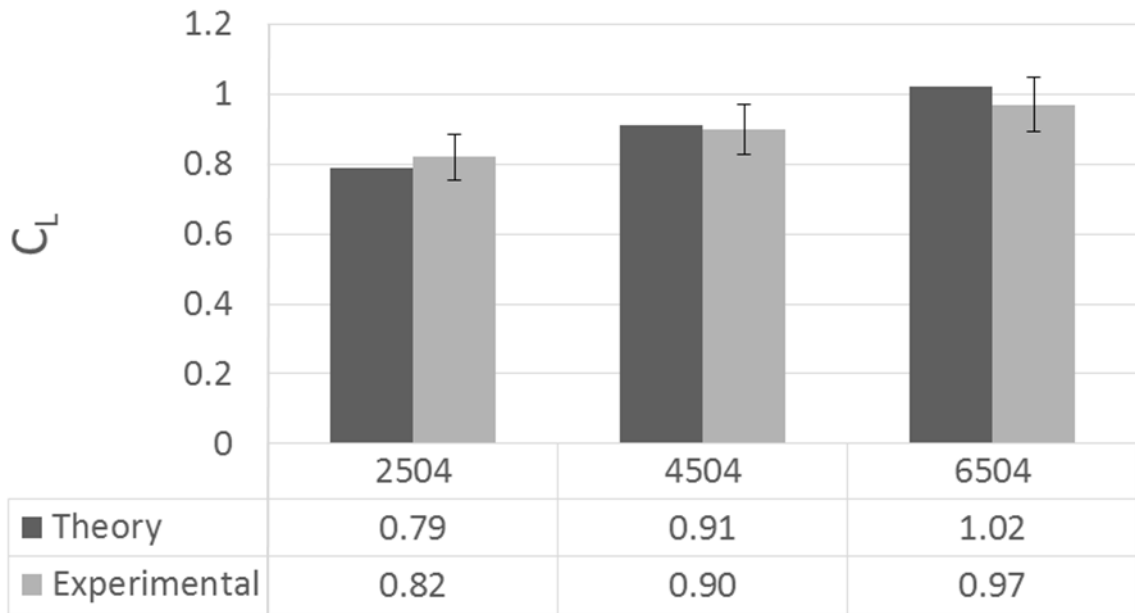


Figure 4.17. Lift coefficient at 18°

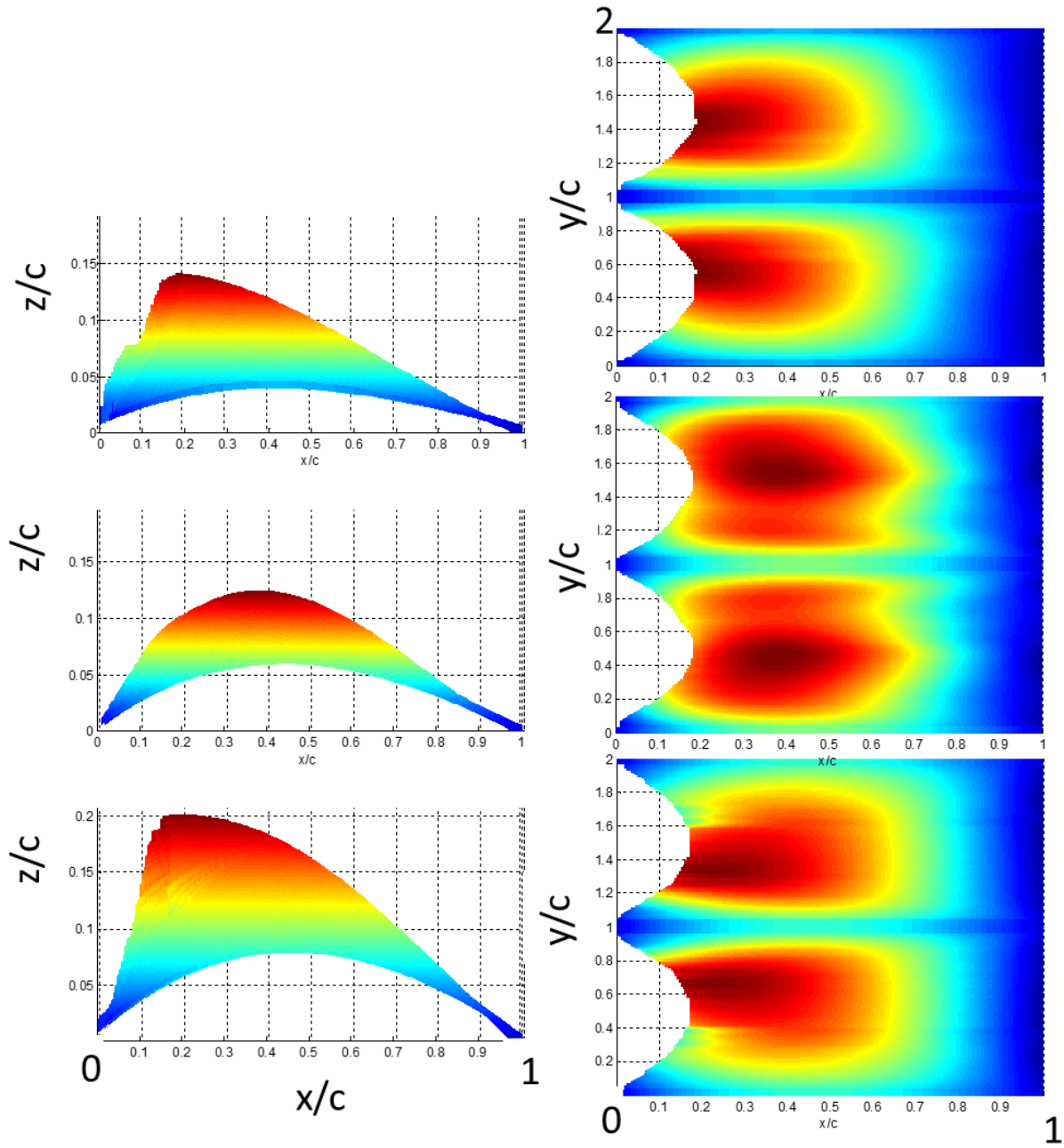


Figure 4.18. Time-averaged shapes at 18° (side view on left, top view on right). From top to bottom: 2504, 4504, 6504. Flow is from right to left

The results for the theoretical lift coefficient indicate that using lifting-line theory for analysis of the measured time-averaged shapes for membrane wings is a reasonable first-order method for approximating lift for those wings despite the limiting assumptions of the theory. This shows the importance of the bound vorticity of the wings relative to the time-averaged shape. As shown in flow field measurements [8, 11, 29], the membrane vibration is necessary to decrease the effects of flow separation, making the analysis a viable estimation tool. Issues with larger displacements and complex cambering observed near the leading edge of the 6504 in Figure 4.15 highlights limitations. Gordnier's theoretical model [26] showed the reduction in separation due to the fluid-structure interaction between the membrane and flow over the wing. Similarly, these studies have shown that lift is enhanced due to the membrane's flexibility, especially at higher angles-of-attack due to the dynamic interaction between the flow and membrane in addition to the mean camber. In this case, additional camber is generated due to the camber of the frame.

Initial frame camber has a noticeable effect on membrane camber. This is apparent with the membrane wing side views shown in Figure 4.19. In the plots, the green line represents the adjusted chord line for the blue spanwise-averaged lines. The adjusted chord line intersects the leading edge tip of the wing and the maximum scallop point of the trailing edge of the membrane. The distance between the adjusted chord line and the maximum membrane displacement location normal to the adjusted chord line, dz' , is used to represent the added camber. Referring to the top views of Figures 4.16 and 4.18, this additional membrane camber is heavily influenced by larger displacements closer to the mid-span of the wings. The average geometric twist was determined from the slope of the adjusted chord line. These were -2.5° , -

5.9°, -4.2°, and -6.5° for the flat, 2504, 4504, and 6504 airfoils, respectively. While the average twist does not show a clear relation with increasing frame camber, it does show that frame camber causes a more negative effective angle-of-attack than no frame camber.

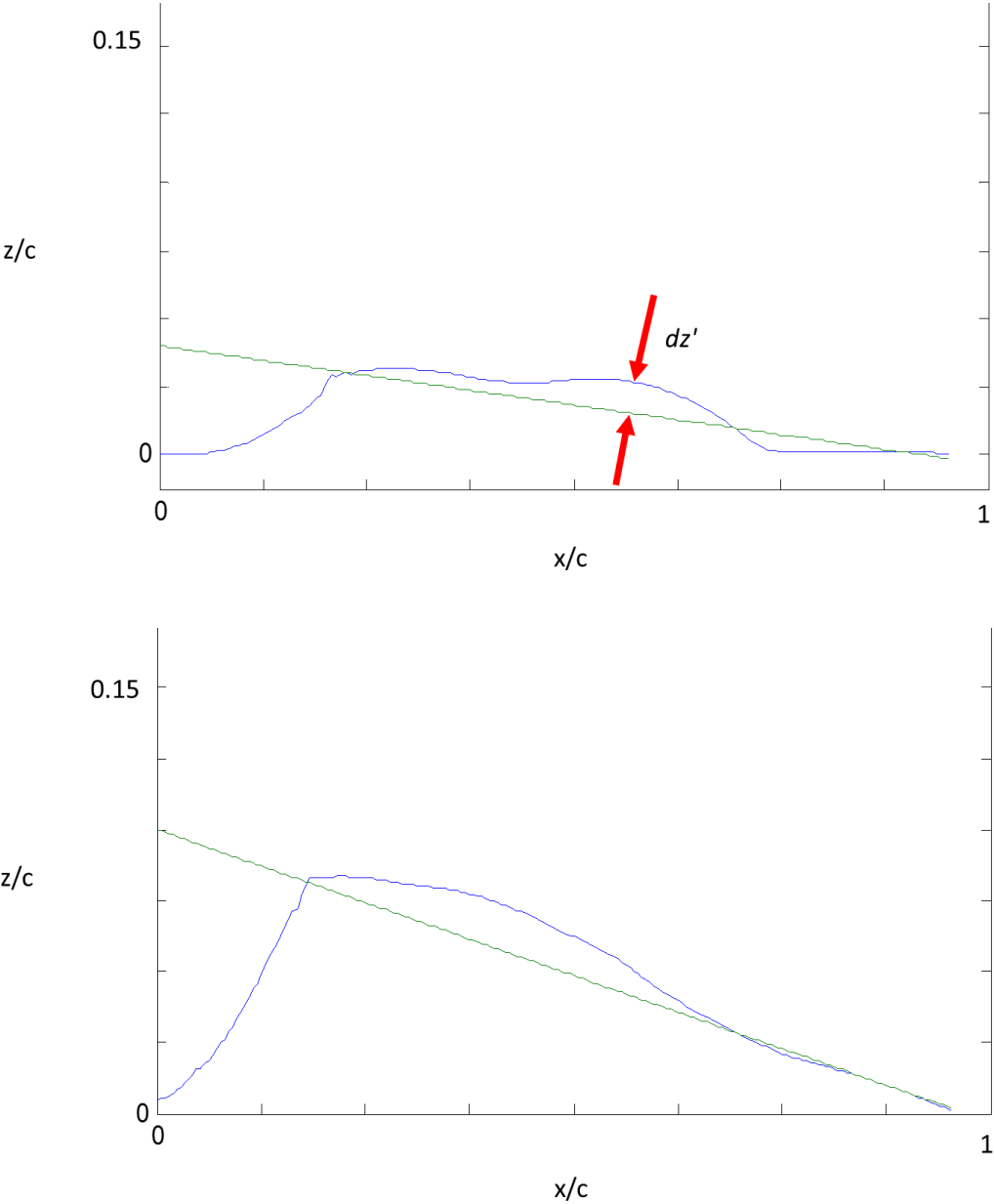


Figure 4.19. a) Time-averaged and spanwise-averaged shape side views for membrane wings from top to bottom: flat and 2504 airfoils. Flow is from right to left

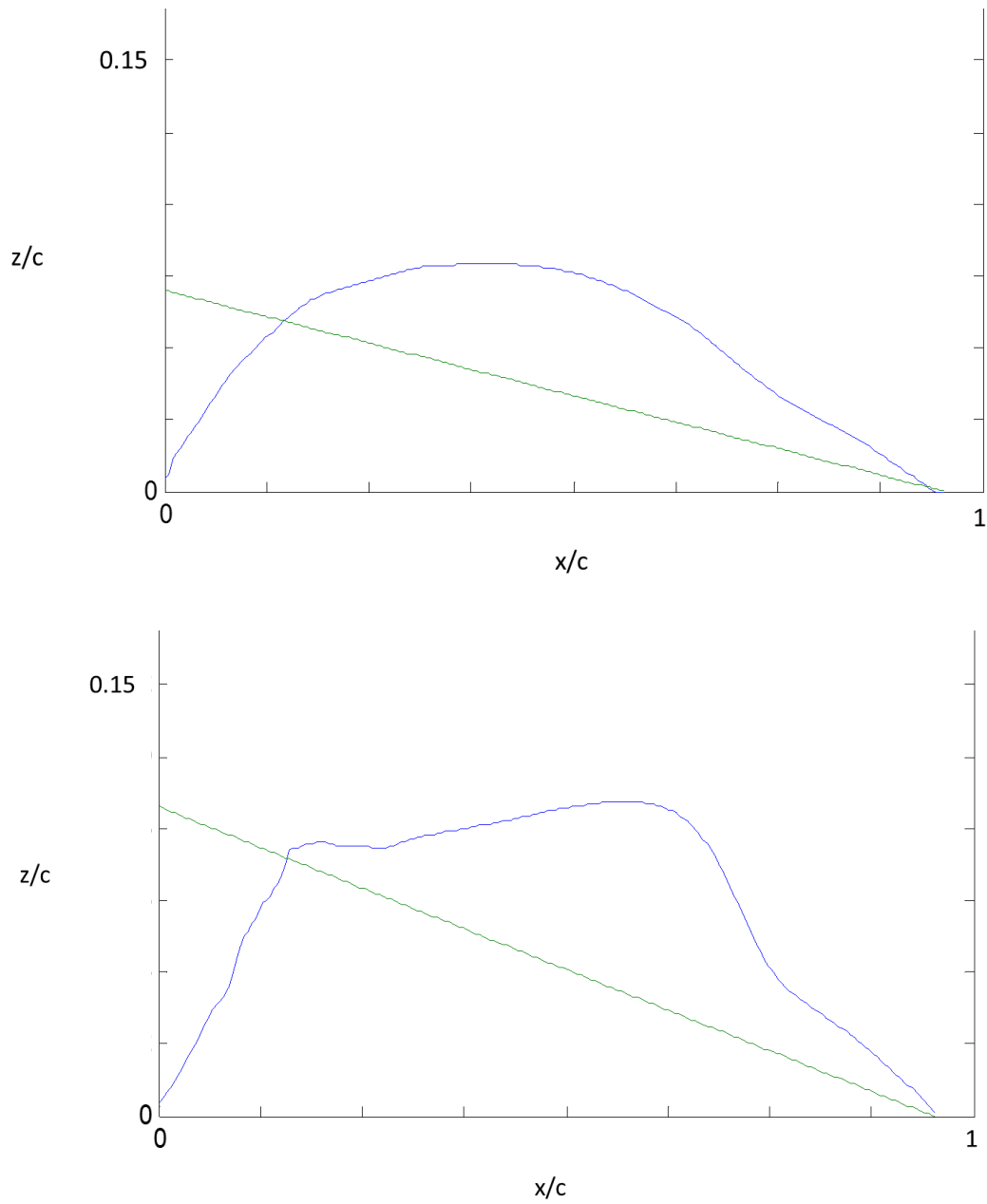


Figure 4.19. b) Time-averaged and spanwise-averaged shape side views for membrane wings from top to bottom: 4504 and 6504 airfoils. Flow is from right to left

The added membrane camber, dz' , was quantified and plotted relative to $C_{L,max}$, Figure 4.19. The plot shows a monotonic increase in $C_{L,max}$ and additional membrane camber as frame

camber increases. Increasing the frame camber effectively increases the lift, which in turn increases the membrane deflection, demonstrating an amplifying effect with diminishing returns due to the increased aerodynamic tensioning of the membrane.

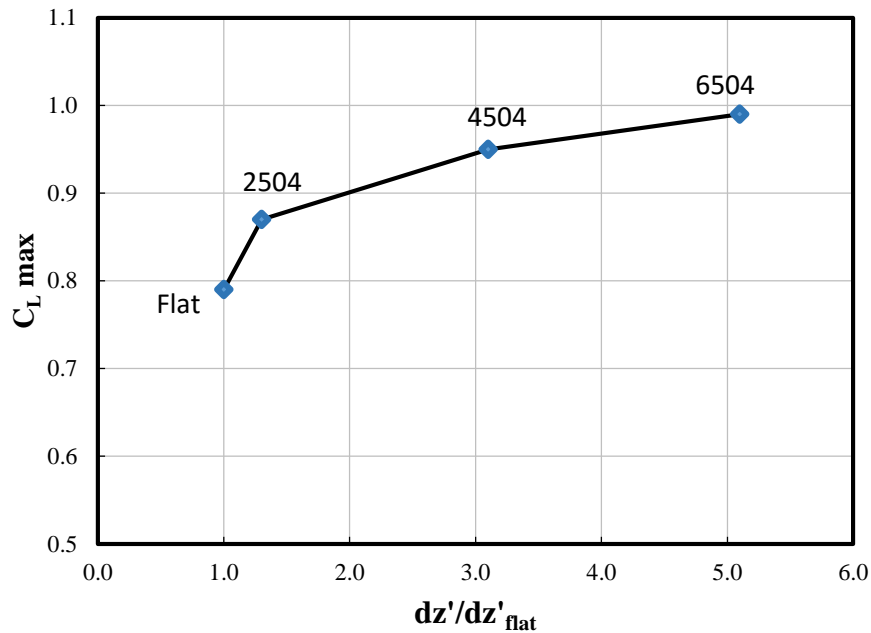


Figure 4.20. $C_{L,max}$ vs additional membrane camber

As previously discussed (Eq. 4.6), lifting-line analysis also enables a calculation of the induced drag coefficient. Because the lift coefficient results were reasonable estimations of the experimental results, it is of interest to estimate the induced drag component of the overall measured drag. Results are presented in Table 4.1. At low angle-of-attack (high aerodynamic efficiency), the induced drag comprises 11-20% of the total drag. At high angle-of-attack (high lift coefficient), as expected, the induced drag is a higher contributor at 32-45% due to the higher

lift coefficient and the subsequently stronger tip vortices. Trends for the induced drag percentage indicate that increasing frame camber decreases the effect of induced drag.

Table 4.1. Induced Drag Calculations

	2504			4504			6504		
α	$C_{D,i}$	$C_{D,exp}$	Ratio	$C_{D,i}$	$C_{D,exp}$	Ratio	$C_{D,i}$	$C_{D,exp}$	Ratio
6	0.01	0.05	20%	0.01	0.06	17%	0.01	0.09	11%
18	0.10	0.24	42%	0.10	0.22	45%	0.08	0.25	32%

Based on the DIC and theoretical analyses, lifting-line theory does a reasonably good job of approximating the lift for each wings when compared to the experimental values, with the one exception being a case where the time-averaged shape exhibited considerable negative cambering near the leading-edge. Additionally, an increase in induced drag percentage (of total drag) was calculated by theory as angle-of-attack increased from 6° to 18°. Moreover, increasing frame camber also results in increased aero-induced membrane camber relative to the adjusted chord line.

CHAPTER 5. CONCLUSIONS

In this study, low aspect ratio, flexible MAV wings with cambered and flat frames were designed, fabricated, and tested to determine whether cambered frames provide membrane wings with aerodynamic advantages when compared to those with flat frames. The frames were modeled in SolidWorks and constructed using an Objet30 Pro 3D printer with an aspect ratio of 2. The membranes were composed of a silicone rubber material. The wings were tested in an MAV low speed wind tunnel at a Reynolds number of 50,000 (10 m/s) while varying angles-of-attack from -4 to 24° . A load cell was used to gather force and moment measurements. From the force and moment measurements, plots were developed for lift, drag, and pitching moment coefficients vs angle-of-attack. By analyzing the resulting plots for aerodynamic forces and moments, the following conclusions are made:

- 1) Frame cambering had a 20% larger effect than maximum camber location or frame thickness on aerodynamic coefficients for $AR = 2$ membrane wings.
- 2) At angles-of-attack greater than 10° , as the lift curve slope starts to decrease, all of the membrane wings with cambered frames displayed greater lift than that of the flat frames.
- 3) With the exception of the 6% cambered frame and 6% thickness, the membrane wings with cambered frames produced 10-20% less drag than flat frames.

- 4) L/D and endurance measurements for the membrane wings with cambered frames were superior to that of the flat frames by up to 60%.
- 5) Increasing frame camber further decreases the pitching moment, and the aerodynamic center is near the quarter-chord.

In addition to the experimental force and moment coefficients, a DIC camera system was used to acquire time-averaged shapes for the membrane wings during wind tunnel tests. The wings were mounted vertically at angles-of-attack of 6° and 18° to represent the regions of maximum efficiency and approaching stall, respectively. A total of 100 images were acquired with each configuration. An in-house MATLAB program was developed to average the deflection plots from the images and produce time-averaged shapes. Lifting-line theory was applied to the time-averaged shape to calculate theoretical lift and induced drag coefficients. The calculations required inputs such as the local chord length and geometric twist—both of which were determined from the geometries of time-averaged shapes. From the analysis of the time-averaged shapes, the following conclusions are made:

- 1) Applying lifting-line theory to time-averaged shapes of membrane wings does a reasonably good job of approximating lift coefficients and capturing the effects of bound vorticity despite the low Re , low AR environment. One exception was where considerable negative cambering is exhibited near the leading edge.
- 2) The ratio of induced drag to total drag increased for the membrane wings as the angle-of-attack was changed from 6° to 18° .

- 3) Increasing frame camber results in increased aero-induced membrane camber relative to the adjusted chord line.

REFERENCES

1. Pines, D. and Bohorquez, F. "Challenges Facing Future Micro-Air-Vehicle Development," *Journal of Aircraft*, Vol. 43, No. 2, 2006.
2. Mueller, T. J. *Fixed and Flapping Wing Aerodynamics for Micro Air Vehicle Applications*, American Institute of Aeronautics & Astronautics, 2001.
3. Wissa, A, Grauer, J, Guerreiro, N, Hubbard Jr., J, Altenbuchner, C, Tummala, Y, Frecker, M, Roberts, R. "Free Flight Testing and Performance Evaluation of a Passively Morphing Ornithopter," *International Journal of Micro Air Vehicles*, Vol. 7 No. 1. 2015.
4. Woods, M. I., Henderson, J. F., and Lock, G. D. "Energy requirements for the flight of micro air vehicles," *Aeronautical Journal* Vol. 105, No. 1045, 2001, pp. 135-149.
5. Bakhtian, N.M., Babinsky, H., Thomas, A.L.R., and Taylor, G.K. "The Low Reynolds Number Aerodynamics of Leading Edge Flaps," *45th AIAA Aerospace Sciences Meeting and Exhibit*, Reno, Nevada, January, 2007, AIAA 2007-662.
6. Song, A, Tian, X, Israeli, E, Galvao, R, Bishop, K, Swartz, S, and Breuer, K. "Aeromechanics of Membrane Wings with Implications for Animal Flight," *AIAA Journal*, Vol. 46, No. 8, August 2008.
7. Ifju, P. G., Jenkins, D. A., Ettinger, S., Lian, Y., and Shyy, W. "Flexible-wing-based micro air vehicles," *40th AIAA Aerospace Sciences Meeting & Exhibit*, 2002, AIAA 2002-0705.
8. Albertani, R., Stanford, B., Hubner, J. P., and Ifju, P. G. "Aerodynamic coefficients and deformation measurements on flexible micro air vehicle wings," *Experimental Mechanics*, Vol. 47, No. 5, 2007, pp. 625-635.
9. Hu, H., Tamai, M., and Murphy, J. T. "Flexible-Membrane Airfoils at Low Reynolds Numbers," *Journal of Aircraft*, Vol. 45, No. 5, 2008, pp. 1767-1778.
10. Mastramico, N. J., and Hubner, J. P. "A Study of the Wake Characteristics for Membrane Flat and Cambered Plates," *26th AIAA Aerodynamic Measurement Technology and Ground Testing Conference*, Seattle, Washington, 2008, pp. AIAA 2008-4369.
11. Timpe, A., Zhang, Z., Hubner, J., and Ukeiley, L. "Passive flow control by membrane wings for aerodynamic benefit," *Experiments in Fluids*, Vol. 54, No. 3, 2013.

12. Zhang, Z. "Static and Dynamic Characteristics of Membrane Wings at Low Reynolds Number," *Dissertation, Department of Aerospace Engineering and Mechanics, The University of Alabama*, 2014.
13. Arce, M. A. and Ukeiley, L. "Fluid Structure Interactions in Low Aspect Ratio Membrane Wings," *17th International Symposium on Applications of Laser Techniques to Fluid Mechanics*, Lisbon, Portugal, 07-10 July, 2014.
14. Zhang, Z., Martin, N., Wrist, A., and Hubner, J.P., "Force and Deformation Measurement of Low Aspect Ratio Membrane Airfoils," *2013 AIAA Science and Technology*, 2013-0682.
15. Hubner, J.P. and Hicks, T., "Trialing Edge Scalloping Effect on Flat-Plate Membrane Wing Performance," *Aerospace Science and Technology*, 15 Vol. 15, No. 8, Dec, 2011, pp. 670-680.
16. Scott, K. D., Hubner, J. P., and Ukeiley, L. "Cell Geometry and Material Property Effects on Membrane and Flow Response," *AIAA Journal*, Vol. 50, No. 3, 2012, pp. 755-761.
17. Abudaram, Y., Stanford, B., and Ifju, P. "Wind Tunnel Testing of Load-Alleviating Membrane Wings at Low Reynolds Numbers," *47th AIAA Aerospace Sciences Meeting including The New Horizons Forum and Aerospace Exposition*, 2009, pp. AIAA 2009-1468.
18. Zimmerman, C. H. "Aerodynamic characteristics of several airfoils of low aspect ratio." *National Advisory Committee for Aeronautics*, 1935.
19. Mueller, T. J. "Aerodynamic Measurements at Low Reynolds Numbers for Fixed Wing Micro-Air Vehicles," *RTO AVT/VKI Special Course*, 1999.
20. Pelletier, A., and Mueller, T. J. "Low Reynolds number aerodynamics of low-aspect-ratio, thin/flat/cambered-plate wings," *Journal of Aircraft*, Vol. 37, No. 5, 2000, pp. 825-832.
21. Torres, G. E., and Mueller, T. J. "Low-Aspect-Ratio Wing Aerodynamics at Low Reynolds Numbers," *AIAA Journal*, Vol. 42, No. 5, 2004, pp. 865-875.
22. Mizoguchi, M., and Itoh, H. "Effect of Aspect Ratio on Aerodynamic Characteristics at Low Reynolds Numbers," *AIAA Journal*, Vol. 51, No. 7, 2013, pp. 1631-1639.
23. Waszak, M.R., Jenkins, L.N., Ifju, P. "Stability and Control Properties of an Aeroelastic Fixed Wing Micro Aerial Vehicle," *AIAA Atmospheric Flight Mechanics Conference and Exhibit*, Montreal, Canada, August, 2001, AIAA 2001-4005.
24. Jenkins, D. A., Ifju, P. G., Abdulrahim, M., and Olipra, S. "Assessment of Controllability of Micro Air Vehicles," *16th Bristol International RPV/UAV Conference*, 2001, p. Paper 30.
25. Johnston, J. W., Romberg, W., Attar, P. J., and Parthasarathy, R. "Experimental Characterization of Limit Cycle Oscillations in Membrane Wing Micro Air Vehicles," *Journal of Aircraft*, Vol. 47, No. 4, 2010, pp. 1300-1308.
26. Gordnier, R. E., and Attar, P. J. "Aeroelastic Simulations of an Aspect Ratio Two Flexible Membrane Wing," *50th AIAA Aerospace Sciences Meeting including the New Horizons Forum and Aerospace Exposition*, Nashville, Tennessee, 2012, pp. AIAA 2012-0711.

27. Zhang, Z., Hopper, L., Wrist, A., Hubner, J. P., and Ukeiley, L. "Nondimensional frequency scaling of aerodynamically-tensioned membranes," *Journal of Fluids and Structures*, Vol. 48, No. 0, 2014, pp. 14-26.
28. Specification Sheet: Polyjet Materials Data Sheet, Stratasys, 2015.
29. Bertin, J.J. and Smith, M.L. *Aerodynamics for Engineers*, 3rd ed. Prentice Hall, Inc. 1998.
30. Okamoto, M., and Azuma, A. "Aerodynamic Characteristics at Low Reynolds Numbers for Wings of Various Planforms," *AIAA Journal*, Vol. 49, No. 6, 2011, pp. 1135-1150.
31. Bolonkin, A., and Gilyard, G. B. "Estimated Benefits of Variable-Geometry Wing Camber Control for Transport Aircraft," NASA/TM-1999-206586, Oct. 1999.

APPENDIX

MATLAB CODE

A.1 OFFSET LOAD CELL ANGLE CALCULATION

```
%Finds Load cell offset angle for wind tunnel test
%Created by: Andrew Wrist
%June, 2014

clc
clear all
close all

x = linspace(-5,30,50000);
a = importdata('LCtest.txt'); %import load cell test data
alpha = a.data(1:9,1); %angle-of-attack data
fx = a.data(1:9,15); %Fx data
b = polyfit(alpha,fx,1);
c = b(1,1)*x+b(1,2);
cabs = abs(c);
minc = min(cabs);
loc = find(cabs==minc);
LCangle = -x(loc) %offset load cell angle
fprintf('degrees\n\n')

plot(alpha,fx,'s',x,c) %plots Fx vs alpha
axis([-5 5 -.05 .05])
xlabel('alpha')
ylabel('fx')
grid on
```

A.2 DIC TIME AVERAGE AND LIFTING LINE THEORY

```
%DIC time-averaged membrane shape and Lifting Line theory
calculation
%By: Andrew Wrist
%2015

clc
clear all
format compact
qq = 1;
B = zeros;
AVX = zeros;
alpha = 6; %angle of attack
AR = 2*(.1524*.0762)^2/.0101^2; %Aspect ratio including scallop

%Import and process displacement matrices
for n = 5:101
    A = zeros;

    %Import displacement matrices
    name = ['(2)6Deg4504NACA-' num2str(n, '%04i') '_0.mat'];
    load(name);
    sz = size(W);
    rows = sz(1);
    col = sz(2);
    C = W;

    %Averaging process
    for i = 1:col
        avx(i) = mean(C(10:rows-10,i));
    end
    for i = 1:col
        for m = 1:rows
            if W(m,i)==0
                W(m,i) = NaN;
            end
        end
    end
end
A = W;
B = (B*(qq-1)+A)/qq; %averaging step
```

```

xx = linspace(0,76.2,rows);
yy = linspace(0,76.2,col);

figure(2) %plot of membrane shape during averaging process
surf(yy, xx, B, 'edgecolor', 'none')
zlim([-1 20])
pause (.01)
qq = qq + 1;
end

%Smooth shape and get rid of zeros
sm = W;
meanmatrix = W;
for i = 3:rows-2
    for j = 3:col-2
        minimn = [sm(i-2,j-2) sm(i-2,j-1) sm(i-2,j)...
            sm(i-2,j+1) sm(i-2,j+2);...
            sm(i-1,j-2) sm(i-1,j-1) sm(i-1,j)...
            sm(i-1,j+1) sm(i-1,j+2);...
            sm(i,j-2) sm(i,j-1) sm(i,j)...
            sm(i,j+1) sm(i,j+2);...
            sm(i+1,j-2) sm(i+1,j-1) sm(i+1,j)...
            sm(i+1,j+1) sm(i+1,j+2);
            sm(i+2,j-2) sm(i+2,j-1) sm(i+2,j)...
            sm(i+2,j+1) sm(i+2,j+2)];
        meanmatrix(i,j) = nanmean(nanmean(minimn));
    end
end
C = W;
B = meanmatrix;

%4504 Frame and offset slope correction
for basecoords = 1:1
    base = [1.000000 0.000420 %4504 airfoil coordinates.
    Changed for
        0.998459 0.000738 %different airfoils
        0.993844 0.001686
        0.986185 0.003241
        0.975528 0.005367
        0.961940 0.008017
        0.945503 0.011130
        0.926320 0.014637
        0.904508 0.018458
        0.880203 0.022509
        0.853553 0.026702
        0.824724 0.030946
        0.793893 0.035149

```

0.761249	0.039221
0.726995	0.043077
0.691342	0.046634
0.654508	0.049819
0.616723	0.052566
0.578217	0.054815
0.539230	0.056521
0.500000	0.057647
0.460770	0.058167
0.421783	0.058071
0.383277	0.057357
0.345492	0.056039
0.308658	0.054142
0.273005	0.051705
0.238751	0.048777
0.206107	0.045418
0.175276	0.041698
0.146447	0.037694
0.119797	0.033489
0.095492	0.029169
0.073680	0.024822
0.054497	0.020533
0.038060	0.016384
0.024472	0.012451
0.013815	0.008798
0.006156	0.005480
0.001541	0.002538
0.000000	0.000000
0.001541	-0.002046
0.006156	-0.003522
0.013815	-0.004438
0.024472	-0.004811
0.038060	-0.004669
0.054497	-0.004045
0.073680	-0.002982
0.095492	-0.001530
0.119797	0.000253
0.146447	0.002306
0.175276	0.004559
0.206107	0.006942
0.238751	0.009383
0.273005	0.011806
0.308658	0.014142
0.345492	0.016322
0.383277	0.018284
0.421783	0.019972
0.460770	0.021340

```

0.500000  0.022353
0.539230  0.022986
0.578217  0.023227
0.616723  0.023075
0.654508  0.022541
0.691342  0.021650
0.726995  0.020435
0.761249  0.018939
0.793893  0.017212
0.824724  0.015311
0.853553  0.013298
0.880203  0.011233
0.904508  0.009182
0.926320  0.007204
0.945503  0.005358
0.961940  0.003699
0.975528  0.002272
0.986185  0.001119
0.993844  0.000272
0.998459 -0.000246
1.000000 -0.000420];

end
base = base*76.2;
b = polyfit(base(1:40,1),base(1:40,2),4);
basex = yy;
basey =
b(1).*basex.^4+b(2).*basex.^3+b(3).*basex.^2+b(4).*basex+b(5);
basefull = zeros(rows,col);
slopex = 2.5;
basexslope = linspace(slopex,0,col);
for i = 8:rows-8
    basefull(i,:) = basey-basexslope;
end
for i = 1:7
    B(i,:) = basey;
end
for i = rows-7:rows
    B(i,:) = basey;
end
Bnew = basefull+B;
for i = 1:col
    avx(i) = nanmean(Bnew(1:rows,i));
end
yy = yy/76.2;
xx = xx/76.2;
Bnew = Bnew/76.2;

```

```

%Plot smoothed time-averaged membrane shape with frame
figure(10)
surf(yy,xx,Bnew,'edgecolor','none')
zlim([0 .3])
xlabel('x/c')
zlabel('z/c')
ylabel('y/c')

%Build full wing (both sides)
fullwing(1:2*rows,1:col) = zeros;
halfwing = Bnew;
halfwing(rows+1:2*rows,1:col) = zeros;
fullwing = halfwing+fullwing;
halfwing = flipud(halfwing);
fullwing = halfwing+fullwing;
for i = 2:2*rows
    fullwing(i,col) = fullwing(1,col);
    fullwing(i,col-1) = fullwing(1,col-1);
end
xxfull = linspace(0,152.4,2*rows)/76.2;

%Plot full wing time-averaged shape
figure(12)
surf(yy,xxfull,fullwing,'edgecolor','none')
zlim([0 .3])
xlim([0 1])
ylim([0 2])
xlabel('x/c')
zlabel('z/c')
ylabel('y/c')

%Span-wise polynomial fit and smoothing process
xmatrix = linspace(0,1,col);
for i = 1:rows*2
    fwnan = isnan(fullwing(i,1:col));
    numnan = sum(fwnan);
    yystart = numnan + 1;
    yyend = numel(yy);
    %camber line coefficients
    ccs5 = polyfit(yy(yystart:yyend),fullwing(i,yystart:col),5);
    ccs3 = polyfit(yy(yystart:yyend),fullwing(i,yystart:col),3);
    cambln5 = polyval(ccs5,yy(yystart:yyend));
    cambln3 = polyval(ccs3,yy(yystart:yyend));
    x21 = linspace(0,1,21);
    excelvalues5 = polyval(ccs5,x21)';

    %Full wing, spanwise scan of polynomial fit

```

```

figure(2)
plot(yy,fullwing(i,1:col),yy(yystart:yyend),cambln3,'r')
ylim([0 .5])
xlim([0 1])

clncount = col - numel(cambln3)+1;
smoothwing(i,clncount:col) = cambln3;
z = smoothwing(i,1:col);

%zero lift aoa
th1 = 0;
for j = 1:col-1
    th2 = acos(1-2*xmatrix(j+1));
    dzdxt(j) = (z(j+1)-z(j))/(xmatrix(j+1)-xmatrix(j));
    aL0(j) = -1/pi()*dzdxt(j)*(sin(th2)-(th2)-(sin(th1)-
(th1)));
    th1 = th2;
end
aL0rad(i) = sum(aL0);
if i>10 && i<col-10
    if abs(aL0rad(i)-aL0rad(i-1))>.5*pi()/180
        aL0rad(i) = aL0rad(i-1); %zero lift AOA in radians
    end
end
end
end

aL0deg = aL0rad'*180/pi(); %zero lift AOA in degrees

%Further smoothing and get rid of zeros
swmod = smoothwing;
for i = 1:col
    for m = 1:rows*2
        if swmod(m,i)==0
            swmod(m,i) = NaN;
        end
    end
end
end

%Surface plot of smoothed wing
figure(3)
surf(yy,xxfull,swmod,'edgecolor','none')
zlim([0 .3])
xlim([0 1])
ylim([0 2])
xlabel('x/c')
ylabel('y/c')
zlabel('z/c')

```

```

%Plot of zero lift AOA vs x/c
figure(4)
plot(xxfull,aL0deg)
xlabel('x/c')
ylabel('Zero lift AOA')

%Geometric twist calculation
xxfullb = xxfull-1;
phi = 180/pi()*acos(-xxfullb); %spanwise location, phi
ao = pi();
b = 2;
for i = 1:rows
    hwnan(i,1:col) = isnan(swmod(i,1:col)); %half wing nan count
    nec(i,1) = sum(hwnan(i,1:col)); %number of empty cells
    c(i,1) = (col-nec(i,1))/col; %chord length at each i
    mu(i) = c(i)*ao/4/b; %mu
    effdiff(i) = swmod(i,nec(i)+1)-swmod(i,col);
    slope(i) = effdiff(i)/(c(i));
    beta(i) = atan(effdiff(i)/c(i));
    betad(i) = beta(i)*180/pi();
    aeff(i) = alpha*pi()/180-beta(i); %Geometric twist in rad
    if i>10 && i<rows-10
        if abs(aeff(i)-aeff(i-1))>.5*pi()/180
            aeff(i) = aeff(i-1);
        end
    end
    aeffd(i) = aeff(i)*180/pi(); %Geometric twist in deg
end

%plot of geometric twist vs x/c
figure(6)
plot(xx,aeffd)
xlabel('x/c')
ylabel('eff AOA')

%Begin building lifting line theory equations
n = 100;
lhs2 = 0;
lhs2(1:n-1,1) = 0;
fnc2 = 0;
fnc2 = zeros(n-1,n-1);
j = linspace(2,rows,n);
for i = 1:n
    j(i) = round(j(i));
end
j(1) = 2;

```

```

j(n) = rows;
phirad= phi*pi()/180;
delta_theta = pi/2/n;

%A Matrix calculation
for i = 1:n-1
    phirad = pi/2-i*delta_theta;
    k = j(i+1);
    lhs2(i) = mu(k)*(aeff(k)-aL0rad(k))*sin(phirad);
    for ii = 1:n-1
        fnc2(i,ii) = sin(((ii-1)*2)+1)*phirad)*(((ii-
1)*2)+1)*mu(k)...
            +sin(phirad));
    end
end
Amatrix = inv(fnc2)*lhs2;
Cl = Amatrix(1)*pi()*AR %Lift coefficient calculation

for i = 1:n-1
    Aratio(i) = Amatrix(i)^2*(i*2-1)/Amatrix(1)^2;
end
Cdv = Cl^2/(pi()*AR)*(sum(Aratio)) %Induced drag coefficient
calculation

%Surface plot with phi locations
figure(5)
surf(yy,phi,swmod,'edgecolor','none')
zlim([0 .3])
xlim([0 1])
ylim([0 180])
xlabel('x/c')
ylabel('z/c')
zlabel('phi')

```

A.3 CIRCULATION TERMS CALCULATION

```
%Circulation terms
%Andrew Wrist
%2016

clc
clear all
close all

%A coefficients calculation
x = linspace(0,pi(),75);
A1 = sin(x);
A3 = .5*sin(3*x);
A5 = .25*sin(5*x);
A7 = .125*sin(7*x);
An = A1+A3+A5+A7;

%plot of A coefficients and summation
figure()
plot(x,A1,x,A3,'+',x,A5,'--',x,A7,'*',x,An,'-+')
xlabel('Span-wise Location (0 to pi)')
ylabel('Circulation')
xlim([0 pi()])
ylim([-0.75 1.25])
legend('A1sin(phi)', 'A3sin(phi)', 'A5sin(phi)', ...
       'A7sin(phi)', 'summation', 'Location', 'eastoutside')
```